

LEVEL II

①

HOLOGRAPHIC INTERFEROMETRIC SURVEY OF BOUNDARY
LAYER TRANSITION IN AN AXISYMMETRIC FREE
CONVECTION THERMAL BOUNDARY LAYER

THESIS

AFIT/GAE/AA/79D-12

Gregory S. Meserve
2nd Lt USAF

DDC
RECEIVED
JAN 29 1980
A

Approved for public release; distribution unlimited.

ORIGINAL CONTAINS COLOR PLATES: ALL DDC
REPRODUCTIONS WILL BE IN BLACK AND WHITE

14

AFIT/GAE/AA/79D-12

6

HOLOGRAPHIC INTERFEROMETRIC SURVEY OF BOUNDARY LAYER TRANSITION IN AN AXISYMMETRIC FREE CONVECTION THERMAL BOUNDARY LAYER

9) Master's THESIS

Presented to the Faculty of the School of Engineering of the Air Force Institute of Technology Air University in Partial Fulfillment of the Requirements for the Degree of Master of Science

12/72

by

10) Gregory S./Meserve B.S. 2nd Lt USAF

Graduate Aeronautical Engineering

11) Dec 79

Accession For
NTIS GRA&I <input checked="" type="checkbox"/>
DDC TAB <input type="checkbox"/>
Unannounced <input type="checkbox"/>
Justification <input type="checkbox"/>
By _____
Distribution/ _____
_____ Codes
_____ and/or
Special <input type="checkbox"/>
A

Approved for public release; distribution unlimited.

012 225 JW

Preface

At first the main objective of this study was to train its author in the field of pulse laser holography. Upon graduation the Air Force Flight Dynamics Lab would take on the student to assist on projects that required optical measurements.

A. G. Havener presented the objective to J. Hitchcock, professor at the AFIT School of Engineering. A meeting of a student and the two men was established and initiated the beginnings of this study.

A heated vertical cylinder with free convection conditions was chosen to be the test subject because experimental data is not known to exist. The results would confirm the numerical theoretical solutions that were available.

The selection of the vertical cylinder provided interesting and informative conclusions, but the main objective was never achieved however. The task of mastering the pulse laser holography equipment was successful but the author will be stationed elsewhere.

I am indebted to A. G. Havener and J. Hitchcock for their time, patience and insight. The experience has enhanced my awareness and knowledge.

Finally, I wish to thank my wife Karen who has witnessed many evenings alone. Our love strengthens as our list of life's experiences continues to grow.

Gregory S. Meserve

Contents

	<u>Page</u>
Preface	ii
List of Figures	iv
List of Symbols	v
Abstract	vi
I. Introduction	1
Background	1
Objectives and Approach	3
II. Equipment	4
III. Theory for Data Collection	10
IV. Development of Mathematical Theory	16
Equation of Motion	16
Energy Equation	20
V. Results and Conclusions	30
Laminar Region	30
Transition Region	37
Future Applications	53
Bibliography	54
Appendix A: Approach for Numerical Solution of Governing System of Equations	56
Appendix B: Error Analysis	60
Vita	62

List of Figures

Figure		Page
1	Internal View of Cylinder	5
2	Ceramic Spacer with Thermocouples	6
3	Composition of Color Filter	6
4	Print of Cylinder and Boundary Layer with Colored Filter in Use	8
5	Arrangement of Optical Components Used to Produce Holograms	9
6	General View of Density Field for Constant X-Plane . .	13
7	Axisymmetric Differential Control Volume for Momentum Integral Equation Derivation, Steady Flow . .	18
8	Differential Fluid Element Outside Boundary Layer . . .	18
9	Axisymmetric Differential Control Volume for Energy Transfers in a Steady State Flow	21
10	Assumed Temperature and Velocity Profiles	25
11	Finite Fringe Interferogram of Laminar Region Encompassing Circular Cylinder	31
12	Quantitative Fringe Shift Data at Radial Distances Y .	32
13	Temperature Profile in Radial Direction Y at X = .227 m	33
14	Comparison of Local Nusselt Number for Cylinder with that for Flat Plate	35
15	Finite Fringe Interferogram of Transition Region Encompassing Circular Cylinder	38
16	Zeroth Fringe Interferogram of Transition Region Encompassing Circular Cylinder	40
17	Finite Fringe Interferogram of Transition Region Encompassing Circular Cylinder	42
18-34	Schlieren Color Photographs of Transition Region . . .	43-51
A-1	Stations for Polynomial Numerical Approximation	58

List of Symbols

Units

c_p	Specific heat at constant pressure	N-m/kgm-C
g	Acceleration of gravity	9.8 m/sec ²
g_c	Newton constant relating force and mass	1 kgm-m/N-sec ²
i	Enthalpy	N-m/kgm
K_{DG}	Dale-Gladstone constant	for air $2.2483 \times 10^{-4} \text{ m}^3/\text{kgm}$
p	Pressure	pascal
r_o	Outer radius of cylinder	m
R	r_o + width of cylinder	m
v_x	Velocity in axial direction	m/sec
δ	Boundary layer thickness	m
λ	Wavelength of light	for ruby laser $6943 \times 10^{-10} \text{ m}$
μ	Viscosity	kgm/m-sec
ν	Kinematic Viscosity	m^2/sec

Subscripts

∞	Evaluated for ambient conditions
e	Exit conditions from C.V. at radial distance R
i	Initial condition
w	Evaluated at cylinder wall

Superscript

$+$	Non-dimensionalized parameter
-----	-------------------------------

Abstract

Unique optical data for the laminar and transition regions of an axisymmetric free convection thermal boundary layer are presented. The boundary layer encompasses a vertically oriented right circular cylinder kept at a constant wall temperature and suspended in a quiescent air environment.

Pulse laser holographic interferometry was used to obtain a measurement of the temperature distribution through the boundary layer. Schlieren methods were used to photograph the boundary layer to provide a qualitative description of the transition region. The eddies of transition flow were the important aspect observed in the schlieren measurements.

An approach is outlined to find an approximate numerical solution for the temperature distribution through the laminar boundary layer. Integral equations are developed for a differential control volume in the boundary layer after which assumed forms of the velocity and temperature distributions are used to reduce the integral equations to first order non-linear differential equations. The differential equations are non-dimensionalized and numerical techniques were used in an attempt to obtain a solution.

Quantitative data from the laminar region resulted in a discrepancy of 34.7 percent between theoretical and experimental evaluation of a local Nusselt number. Qualitative observation of the transition region reveals a fringe reversal phenomena that could possibly be associated with the fundamental mechanics of transition. Furthermore, ^{periodic} vortices or eddies were observed in the transition region.

HOLOGRAPHIC INTERFEROMETRIC SURVEY OF BOUNDARY
LAYER TRANSITION IN AN AXISYMMETRIC FREE
CONVECTION THERMAL BOUNDARY LAYER

I. Introduction

Background

To date, the analyses of boundary layers for vertical cylinders are numerical and are essentially unsupported by experimental data. Two studies that pertain directly to this effort are good examples. In 1956, Sparrow and Gregg (Ref 9) developed a numerical solution for the ratio of vertical cylinder to flat plate Nusselt numbers as a function of axial position, and in 1974, Cebeci (Ref 4), solved the governing system of equations for laminar free convection from the outer surface of a vertical cylinder by using a two-point finite-difference numerical technique. Unfortunately no experimental data are available for comparison and conformation of these numerical solutions.

The lack of experimental data of sensitive flows is due primarily to a lack of adequate instrumentation. Until the development of coherent optical measuring techniques, probing devices had to be used to obtain quantitative field data. When the flow field is sensitive, the intrusion of a probe always makes the measurements suspicious. Optical techniques overcome this difficulty because the beam of laser radiation emitted from a relatively low energy laser (less than one joule, typically) is a non-disturbing probe. The techniques for producing holograms developed shortly after the invention of the laser, and since then steady progress has been made by researchers using holography in conjunction with interferometry to explore many different areas. In gas dynamics, for example, Havener

(Ref 10) and Trolinger (Ref 17) have successfully developed, perfected and applied holography to numerous wind tunnel investigations during the past twelve years.

Objectives and Approach

The objective of this study was to measure temperature distributions within the free convection thermal boundary layer encompassing a vertically oriented circular cylinder. Pulse laser holography was used to produce holograms from which temperatures and Nusselt numbers were extracted. This information was compared to Sparrow's and Gregg's numerical analysis to see how the experimental data agree with the numerical data.

Following an examination of the laminar boundary layer, new and unique data of the transition region were obtained. These data were used in hope of getting a better understanding of the transition process. Also, schlieren photography was used to examine qualitatively the transition boundary layer. Finally, following an integral approach suggested by Eckert (Ref 7), a numerical scheme was devised to predict the temperature distributions, but unfortunately, satisfactory results of this approach are unavailable at this time.

II. Equipment

The vertical cylinder was a polished copper tube six feet in length with a one and five eights inches outer diameter. The cylinder wall was heated uniformly by five internally fixed quartz infrared lamps connected in series. Each lamp was separated by ceramic spacers which give added support to the heating elements and also minimize non-uniform convection heating inside the cylinder. A 220 volt variac was used to control the cylinder wall temperature by regulating the voltage supplied to the lamps. Schematic diagrams of the cylinder and a ceramic spacer are shown in Figs 1 and 2, respectively.

Thermocouples of chromel - alumel are imbedded in copper rods inserted in five of the ceramic spacers. The rods were spring loaded and have rounded polished contact points that help provide good thermal contact between the copper rods and the inside cylinder wall. The thermocouples are positioned circumferentially at 45 degree spacings around the cylinder axis, and an ice bath is used for the reference junction.

A Hi-Cam high speed motion picture camera was used in conjunction with a regular Toepler schlieren system to obtain a history of the flow in the transition and turbulent regions. The camera was set to expose five hundred frames per second and a tricolor filter was used in place of the schlieren knife edge normally used in schlieren systems. The filter was composed of blue, green and red transparent plastic strips (see Fig 3). The width of the green strip was approximately the same as the width of the image of the point light source. In use, a light ray refracted off line will pass through the red or blue strips depending on the direction of refraction and the respective orientation of the filter. For this test,

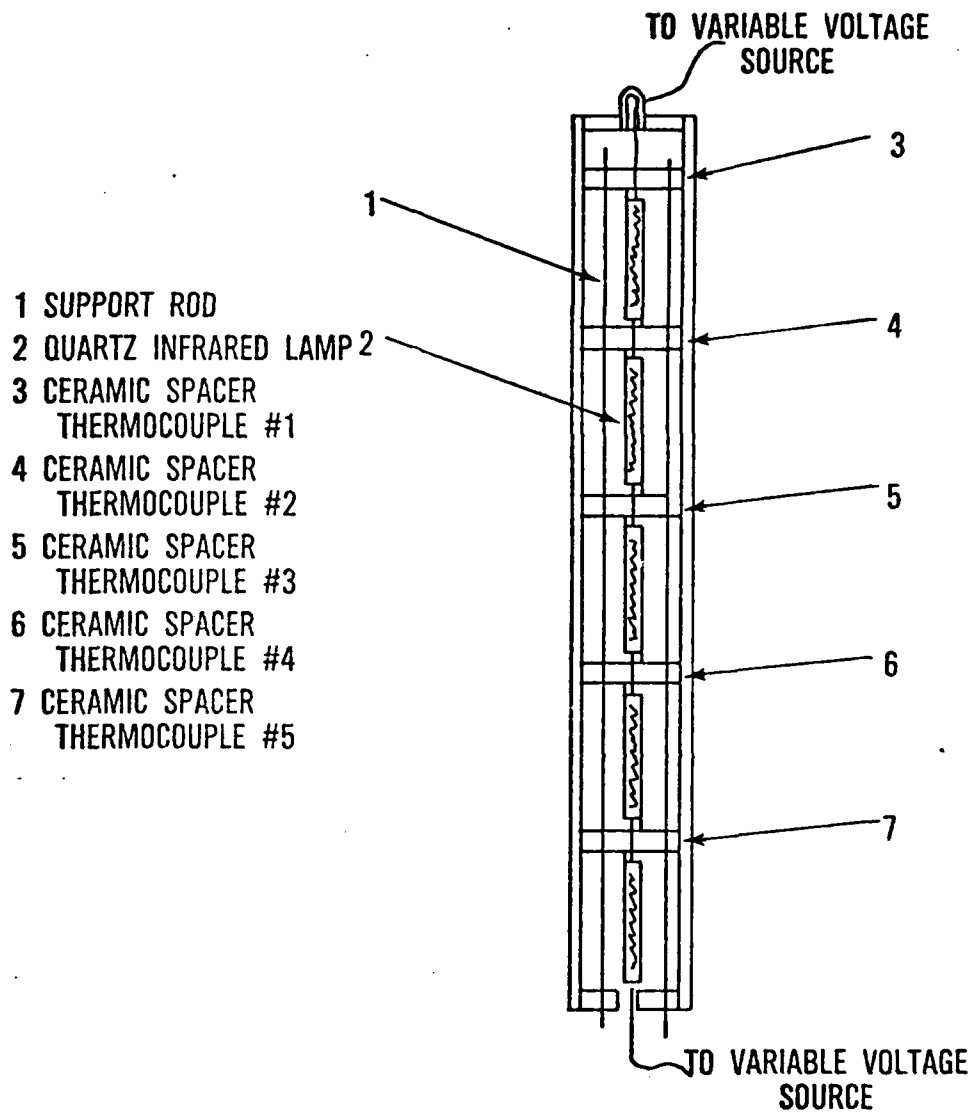


Fig. 1 Internal View of Cylinder

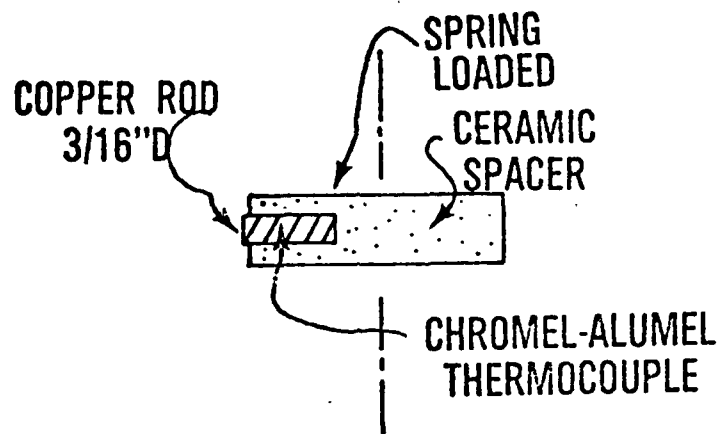


Fig. 2 Ceramic Spacer with Thermocouple

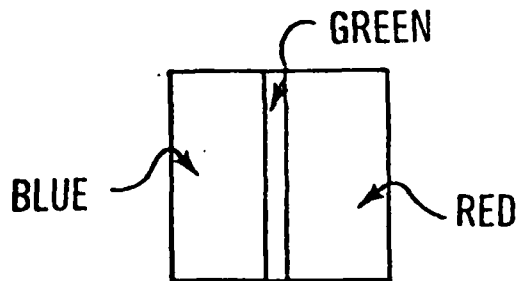


Fig. 3 Composition of Color Filter

the tricolor filter was oriented vertically so that rays traversing the thermal boundary layer pass through either red and blue strips while rays traversing the ambient air pass through the green strip. Then, when the cylinder was photographed with white light, the ambient region appears green while the boundary layer appears red on one side and blue on the other. Figure 4 is a typical example of this result.

The holographic system used in this study was powered by a pulse ruby laser. This system has been in use for more than ten years and is documented in several references (Ref 10).

The cylinder was suspended in the test cabin of a hypersonic wind tunnel. The test cabin can be sealed tightly thereby minimizing environmental disturbances which can easily disrupt the free convection thermal boundary layer. Further, this test cabin has eighteen inch diameter windows which permits large aperture viewing; for this study, it was possible to view eighteen inches of cylinder at one time. The complete system schematic diagram is shown in Fig 5.

2

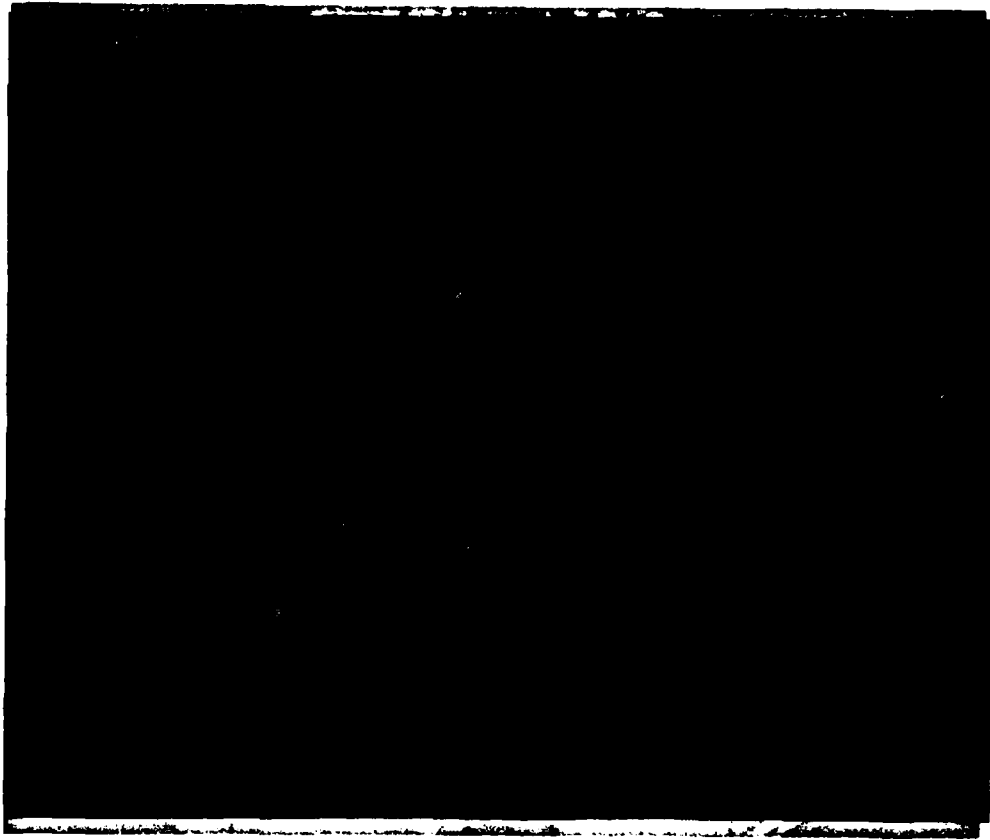


Fig. 4 Print of Cylinder and Boundary Layer with Colored Filter In Use

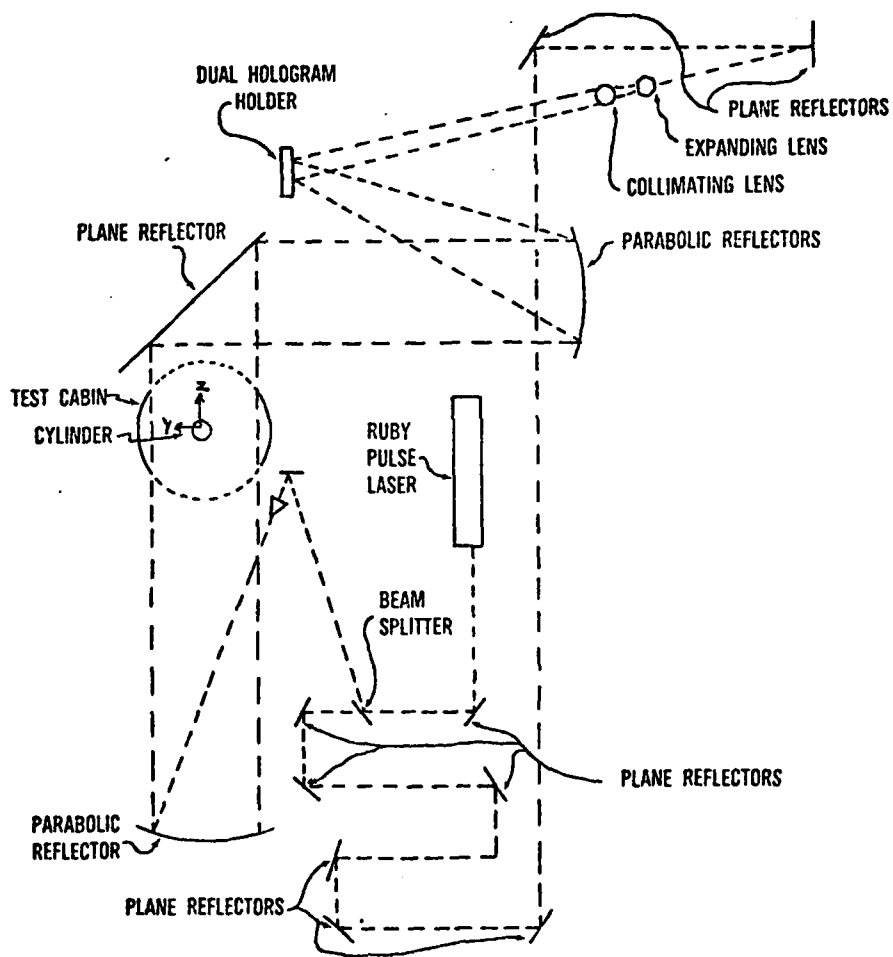


Fig. 5 Arrangement of Optical Components Used to Produce Holograms

III. Theory for Data Collection

Interferometry is an optical process that can be used to gather experimental data on refractive index variations in a test specimen and holography is the process that can be used to record the three fundamental properties of light: frequency, intensity and phase. The hologram is a high resolution photographic emulsion in which the full content of a light wave reflected from or transmitted past a subject can be stored. In practice, the following general process is used to produce a hologram. Light from a laser is divided into two separate beams. One beam illuminates the subject which, in turn, reflects or transmits the light to a special film. During the same time, the other beam is used as an optical reference which directly illuminates the same film. After the film is exposed, chemically processed and reilluminated with only the reference beam, a three dimensional image of the subject can be seen.

In dual hologram interferometry, a hologram of the ambient condition and one hologram of the test condition are simultaneously illuminated with the reference beam, thereby producing simultaneous reconstruction of the object waves. The reconstructed ambient waves serve as a reference against which the reconstructed test waves are compared in the formation of the interferogram.

A shift in the phase of a light wave is revealed in an interferogram as a fringe shift. A fringe is a line of constant optical path length and a displacement of a fringe or fringe shift is caused by changes in the relative phase of the light wave. The phase of the wave varies when the wave traverses a volume with a variable refractive index field. For gases, refractive index variations are proportional to density variations

and consequently, interferometry can be used to measure density variations in gases. The governing equation of this process is

$$S_i = G \int_{\ell_i} f(x,y,z) d\ell_i \quad (1)$$

where

$f(x,y,z)$ is the density function $\frac{\rho(x,y,z)}{\rho_{\text{ref}}} - 1$

i is a subscript denoting an arbitrary straight line through the density field

S_i is the optically measured fringe shift corresponding to the i -th line

ℓ_i is the geometric length of the i -th line through the density field

G is an optical constant prescribed by the wavelength of the light, by the composition of the density field, and by the reference density
 $(G = \frac{KDG}{\lambda} \rho_{\text{ref}})$

Equation (1) is used to calculate local density in the boundary layer from interferometric fringe shifts obtained from the holograms.

Analytic solutions of Eqn (1) are possible only when the density field is two-dimensional or axisymmetric which is an important assumption of this investigation. To obtain the density, Eqn (1) must be inverted. Analytical inversion is possible when the number of independent variables in the integrand are reduced to one. Dependence on one of the variables is suppressed by representing the density field as the summation of thin slices (for this case horizontal slices perpendicular to the cylinder axis); within each slice the density depends only upon two variables. A complete

description is obtained by combining the results of all the slices.

Using rectangular cartesian coordinates and letting the x axis coincide with the axis of the cylinder; the density field is sliced into thin planes in the x-direction. In each plane the density depends only upon y and z. The i-th line through the field can be expressed in polar coordinates where r is the distance from the origin (axis of cylinder for this study) and θ is the corresponding view angle (Fig 6). Equation (1) can be written for a slice as

$$S(r, \theta) = G \int_{l_i} f(y, z) dl_i \quad (2)$$

For an axisymmetric density field all views of the field are the same; therefore, dependence on θ is eliminated and Eqn (2) becomes

$$S(r) = G \int_{l_i} f(y, z) dl_i \quad (3)$$

where

$$r = \sqrt{y^2 + z^2} \quad (4)$$

To obtain an analytical solution to Eqn (3) the dependence on either y or z must be eliminated. To accomplish this, the density field is assumed to be refractionless, which means the bending of a light ray from a straight line through the density field can be neglected because this deviation is assumed to be small compared to the width of the field.

Taking R as the distance from the origin to the edge of the boundary layer and θ equal to zero so that r is equal to y, Eqn (3) becomes

$$S(y) = G \int_{y^2}^{R^2} \frac{f(r) dr^2}{\sqrt{r^2 - y^2}} \quad (5)$$

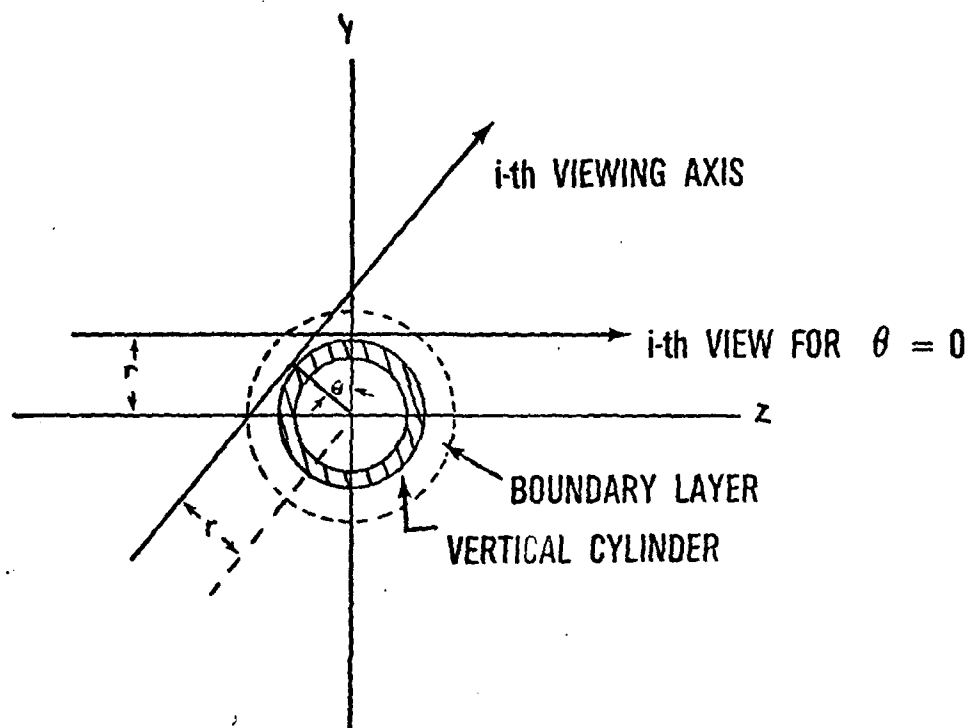


Fig. 6 General View of Density Field For Constant x -Plane

Here, y is constant meaning that the integration is carried out in the z direction only. By using the transformations

$$\xi = 1 - y^2/R^2 \quad (6)$$

$$\eta = 1 - r^2/R^2 \quad (7)$$

Eqn (5) can be expressed as

$$S(\xi) = GR \int_0^\xi \frac{f(\eta) d\eta}{\sqrt{\xi - \eta}} \quad (8)$$

Laplace transformations can be used to invert this convolution integral.

Application of Laplace transformations to Eqn (8) leads to

$$f(\xi) = \frac{1}{GR\sqrt{\pi}} L^{-1} \left\{ \sqrt{s} g(s) \right\} \quad (9)$$

where

$$g(s) = L \left\{ S(\xi) \right\} \quad (10)$$

To obtain the density distribution from this result requires calculation of the Laplace transform of the fringe shift function, $S(\xi)$. A general expression for $S(\xi)$ is obtained from Eqn (8) by assuming a radial distribution for the density. The density in this investigation is assumed continuous so a series solution is assumed for $f(\eta)$,

$$f(\eta) = \sum_{k=0}^m a_k \eta^k \quad (11)$$

and Eqn (8) becomes

$$S(\xi) = GR \int_0^{\xi} \frac{\sum_{k=0}^m a_k \eta^k}{\sqrt{\xi - \eta}} d\eta \quad (12)$$

A term by term evaluation of the integral in Eqn (12) leads to

$$S(\xi) = 2GR \sqrt{\xi} \sum_{k=0}^m k! \xi^k a_k \sum_{i=0}^k \frac{(-1)^i}{(2i+1) i!(k-i)!} \quad (13)$$

or

$$S(\xi) = \sum_{k=0}^m b_k \xi^{k+\frac{1}{2}} \quad (14)$$

Knowing $S(\xi)$, Eqn (10) and Eqn (9) can be used to calculate the density function $f(\xi)$. The result is

$$f(\xi) = \frac{b_0}{2GR} + \frac{1}{2GR} \left[\sum_{i=0}^m \frac{(2i+1)!}{2^{2i} (i!)^2} b_i \xi^i \right] \quad (15)$$

Where the coefficients can be determined from Eqn (14) by using a least squares curve fitting routine to represent the measured $S(\xi)$ values.

For this study the pressure is assumed to be constant across the boundary layer and the air is assumed to behave as an ideal gas. Hence, the temperature through the boundary layer is inversely proportional to the density. When the distribution of density through the boundary layer is known, the temperature distribution can then be determined.

IV. Development of Mathematical Theory

Equation of Motion

In Fig 7 the forces and momentum flux terms that act on a differential control volume are shown. Here

$$dw = \text{weight of fluid in c.v.} = g/g_c \ 2\pi \int_{r_0}^R \rho r dr dx$$

$$(MV)_{in} = \text{momentum flux in} = 2\pi \int_{r_0}^R \rho v_x^2 r dr$$

$$(MV)_{out} = \text{momentum flux out} = 2\pi \int_{r_0}^R \rho v_x^2 r dr + 2\pi \frac{\partial}{\partial x} \int_{r_0}^R \rho v_x^2 r dr dx$$

$$dF_r = \text{shear force} = \tau_w \ 2\pi \ r_0 \ dx$$

$$PA_1 = \text{pressure force acting on surface at } x = 2\pi P \int_{r_0}^R r dr$$

$$PA_2 = \text{pressure force acting on surface at } x + \Delta x$$

$$= 2\pi P \int_{r_0}^R r dr + 2\pi \frac{\partial}{\partial x} \left[P \int_{r_0}^R r dr \right] dx$$

The equation of motion which is derived from Newton's Second Law states that the rate of change of momentum of the fluid passing through the control volume boundary is equal to the sum of the forces acting on the control volume. With regard to normal boundary layer assumptions

($\frac{\partial v_x}{\partial r} \gg \frac{\partial v_x}{\partial x}$ & $\frac{\partial v_r}{\partial x}$ & $\frac{\partial v_r}{\partial r}$) the integral equation of motion is

$$\frac{\partial}{\partial x} \int_{r_0}^R \rho v_x^2 r dr = - \frac{\partial}{\partial x} P \int_{r_0}^R r dr - g/g_c \int_{r_0}^R \rho r dr - \tau_w r_0 \tag{18}$$

For Newtonian fluids the shear stress at the wall is

$$\tau_w = \mu \left(\frac{\partial v_x}{\partial r} \right)_w \quad (19)$$

The pressure gradient is determined by considering a fluid element outside the boundary layer. The pressure terms effecting this differential fluid element are shown in Fig 8. Evaluation of the pressure terms yields

$$\frac{\partial}{\partial x} (P 2\pi r \, dr) \, dx = -g/g_c \rho_\infty \, 2\pi r \, dr \, dx \quad (20)$$

and

$$\frac{\partial P}{\partial x} = -g/g_c \rho_\infty \quad (21)$$

Substituting Eqns (19) and (21) into Eqn (18) yields

$$\frac{\partial}{\partial x} \int_{r_0}^R \rho v_x^2 \, r \, dr = g/g_c \int_{r_0}^R (\rho_\infty - \rho) \, r \, dr + \mu r_0 \left(\frac{\partial v_x}{\partial r} \right)_w \quad (22)$$

From thermodynamics the coefficient of volumetric expansion is defined as

$$\beta = -\frac{1}{\rho} \left(\frac{\partial \rho}{\partial t} \right)_p \quad (23)$$

and for small temperature differences, $\beta \rho \approx \text{constant}$. If the fluid properties are evaluated at a mean boundary layer temperature

$t_m = \frac{1}{2}(t_w + t_a)$ the assumption $\beta \rho \approx \text{constant}$ is better. Integrating, Eqn (23)

$$\rho_\infty - \rho = \beta \rho (t - t_\infty) \quad (24)$$

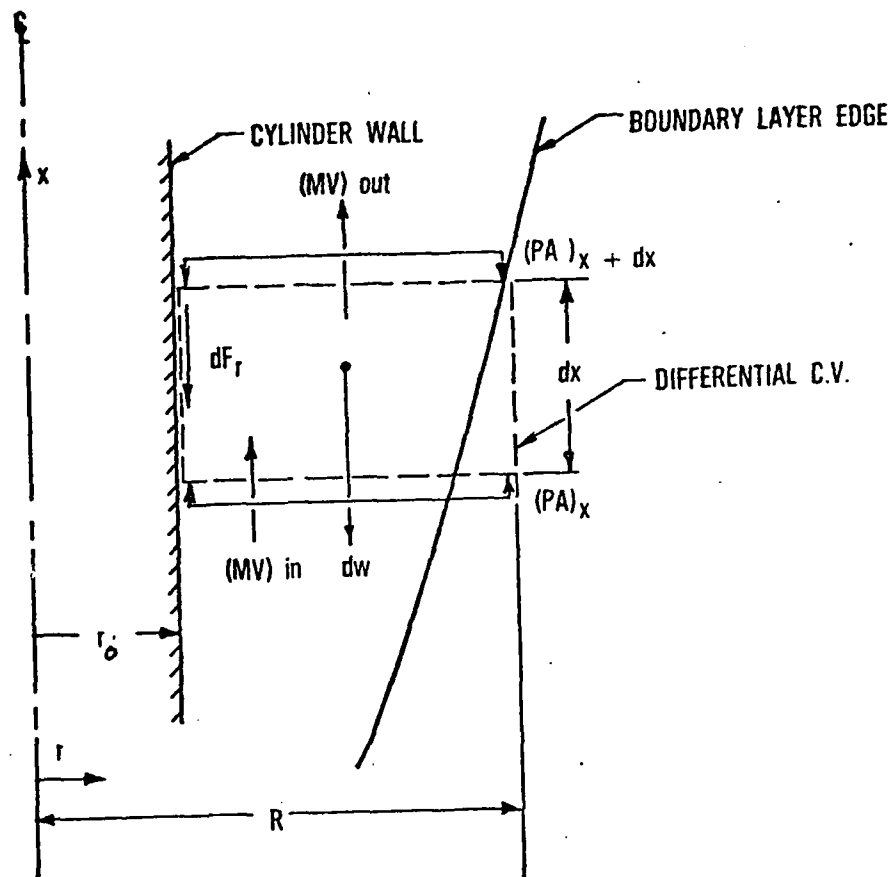


Fig. 7 Axisymmetric Differential Control Volume For Momentum Integral Equation Derivation, Steady Flow

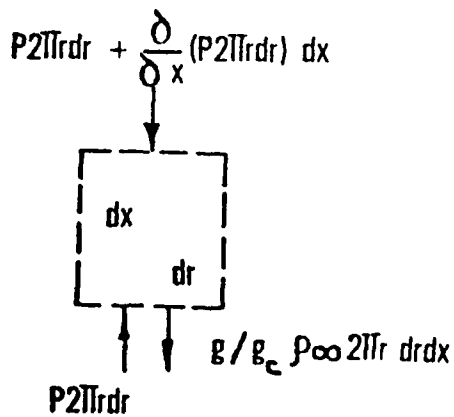


Fig. 8 Differential Fluid Element Outside Boundary Layer

Assuming the flow is incompressible, and substituting Eqn (24) into Eqn (22) leads to

$$\frac{1}{r_0} \frac{\partial}{\partial x} \int_{r_0}^R v_x^2 r dr = \frac{g\beta}{r_0} \int_{r_0}^R (t - t_\infty) r dr - \nu \left(\frac{\partial v_x}{\partial r} \right)_w \quad (25)$$

By defining $y = r - r_0$ the coordinate system is transferred to the surface of the cylinder, and by integrating from the wall to the edge of the boundary layer Eqn (25) becomes

$$\frac{1}{r_0} \frac{\partial}{\partial x} \int_0^\delta v_x^2 (y + r_0) dy = \frac{g\beta}{r_0} \int_0^\delta (t - t_\infty) (y + r_0) dy - \nu \left(\frac{\partial v_x}{\partial y} \right)_w \quad (26)$$

Note that if $y/r_0 \leq .1$ Eqn (27) reduces to the vertical flat plate equation by letting $y \approx 0$.

Energy Equation

For the differential control volume shown in Fig 9, the contributing energy terms and energy flux terms are:

$$\dot{dQ}_{in} = \text{heat transfer rate} = q_w 2\pi r_o dx$$

$$\dot{I}_{in} = \text{rate at which enthalpy is convected into c.v.}$$

$$= 2\pi \int_{r_o}^R \rho v_x i r dr$$

$$\dot{I}_{out} = \text{rate at which enthalpy is convected out of c.v.}$$

$$= 2\pi \int_{r_o}^R v_x i r dr + 2\pi \frac{\partial}{\partial x} \int_{r_o}^R \rho v_x i r dr dx + \rho_e v_e i_e 2\pi R dx$$

The kinetic and potential energy terms of the mass flow into and out of the control volume are neglected assuming that their contribution is small compared to the enthalpy. Furthermore, steady state is assumed and no work is being done.

The energy equation in integral form for this control volume is

$$\frac{1}{r_o} \frac{\partial}{\partial x} \int_{r_o}^R \rho v_x i r dr + \rho_e v_e i_e \frac{R}{r_o} = q_w \quad (27)$$

where the heat flux at the wall is given by Fourier's heat conduction law as

$$q_w = -k \left(\frac{\partial t}{\partial r} \right)_w$$

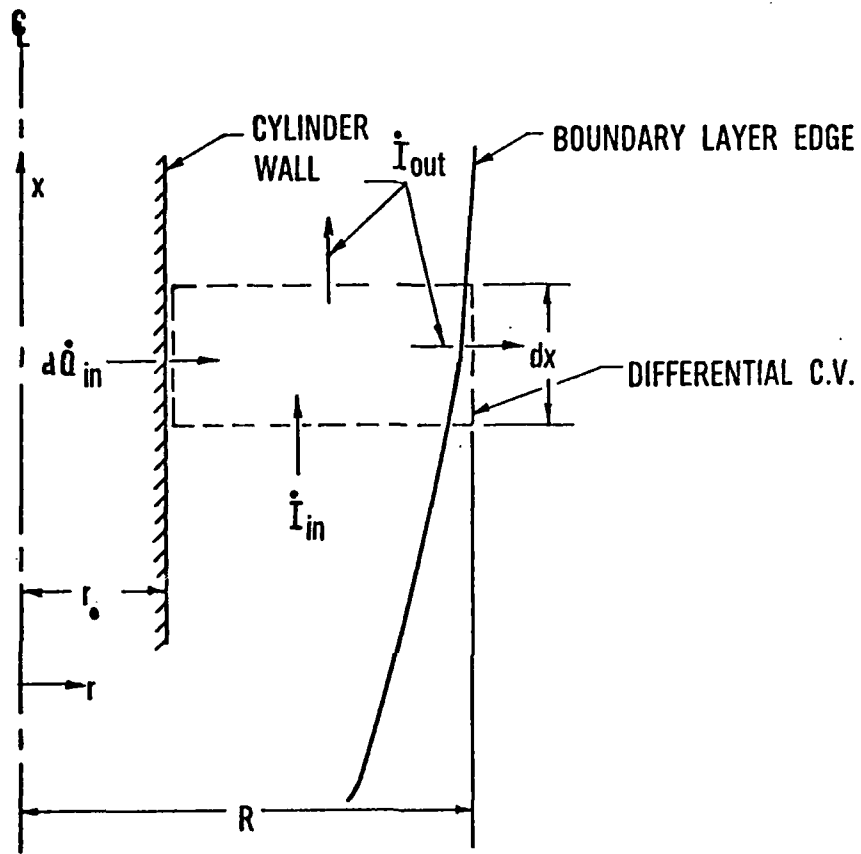


Fig. 9 Axisymmetric Differential Control Volume For Energy Transfers In A Steady State Flow

From the law of conservation of mass applicable to this differential control volume,

$$\rho_e v_e 2\pi R dx = - \frac{\partial}{\partial x} \int_{r_o}^R \rho v_x 2\pi r dr dx \quad (28)$$

and

$$\rho_e v_e = \frac{1}{R} \frac{\partial}{\partial x} \int_{r_o}^R \rho v_x r dr \quad (29)$$

Substituting Fourier's heat conduction law and Eqn (29) into Eqn (27) yields,

$$\frac{1}{r_o} \frac{\partial}{\partial x} \int_{r_o}^R \rho v_x (i - i_e) r dr = -k \left(\frac{\partial t}{\partial r} \right)_w \quad (30)$$

For an ideal gas, enthalpy is a function of temperature only and can be expressed as

$$di = c_p dt \quad (31)$$

Assuming c_p is approximately constant over the temperature range in the boundary layer, integration of Equation (31) leads to

$$i - i_\infty = c_p (t - t_\infty) \quad (32)$$

where $i_\infty = i_e$ and the thermal diffusivity α is, $\alpha = k/\rho c_p$, Eqn (30) can be written as

$$\frac{1}{r_o} \frac{\partial}{\partial x} \int_{r_o}^R v_x (t - t_\infty) r dr = -\alpha \left(\frac{\partial t}{\partial r} \right)_w \quad (33)$$

Using the transformation $y = r - r_0$ as before, integration of Eqn (33) between the wall and the edge of the boundary layer leads to

$$\frac{1}{r_0} \frac{\partial}{\partial x} \int_0^{\delta} v_x (t - t_{\infty}) (y + r_0) dy = - \alpha \left(\frac{\partial t}{\partial y} \right)_w \quad (34)$$

Similar to the equation of motion, note that if $y/r_0 \leq .1$, the energy equation reduces to the vertical flat plate equation by letting $y \approx 0$.

Equations (26) and (34) are a pair of coupled integral equations derived for an axisymmetric, differential control volume. From here, the objective is to transform these integral equations into non-linear first order differential equations. Then, the non-linear first order differential equations are non-dimensionalized. Finally, numerical approximate techniques are used at an attempt to solve the two non-dimensional, non-linear, first order equations simultaneously.

In a theoretical development for a vertical oriented flat plate free convection boundary layer analysis which is similar to the development here, Eckert assumed the form of the velocity and temperature profiles to evaluate the integrals in the pair of coupled flat plate integral equations. The profiles assumed by Eckert will be used here. Accordingly, the velocity profile is

$$v_x = v(y/\delta) (1 - y/\delta)^2 \quad (35)$$

with v being an arbitrary function with the dimensions of velocity. The maximum value of velocity v_x occurs when $y = \delta/3$. At this distance,

$(v_x)_{\max} = 4/27 v$. The boundary conditions of $v_x = 0$ at $y = 0$ and $y = \delta$ are also satisfied. The temperature profile is approximated by the parabola

$$t - t_{\infty} = (t_w - t_{\infty}) (1 - y/\delta)^2 \quad (36)$$

and the boundary conditions $t = t_w$ at $y = 0$ and $t = t_{\infty}$ at $y = \delta$ are also satisfied. These profiles are shown in Fig 10.

Let $\theta = t - t_{\infty}$ and $\theta_w = t_w - t_{\infty}$. Substitution of the velocity and temperature profiles into Eqns (26) and (34) will result in the following first order differential equations. Note that the partial derivatives with respect to x can be written as total derivatives since the variables are functions of x alone. The resulting equation of motion is

$$\frac{1}{280} \frac{d}{dx} \left[v^2 \delta \left(\frac{\delta}{r_0} + \frac{8}{3} \right) \right] = g\beta\theta_w \left[\frac{\delta}{3} \left(\frac{\delta}{4r_0} + 1 \right) \right] - \frac{v\nu}{\delta} \quad (37)$$

and the energy equation is

$$\frac{1}{105} \frac{d}{dx} \left[v\delta \left(\frac{\delta}{r_0} + \frac{7}{2} \right) \right] = \frac{2\alpha}{\delta} \quad (38)$$

Using the non-dimensionalizing factors prescribed by Sparrow and Gregg,

$$\delta^+ = \frac{\delta Gr_x^{1/2}}{x} \quad v^+ = \frac{vx}{\nu Gr_x^{1/2}} \quad x^+ = \frac{x}{r_0 Gr_x^{1/2}}$$

where the Grashof number, Gr , is

$$Gr_x = \frac{g\beta\theta_w x^3}{\nu^3}$$

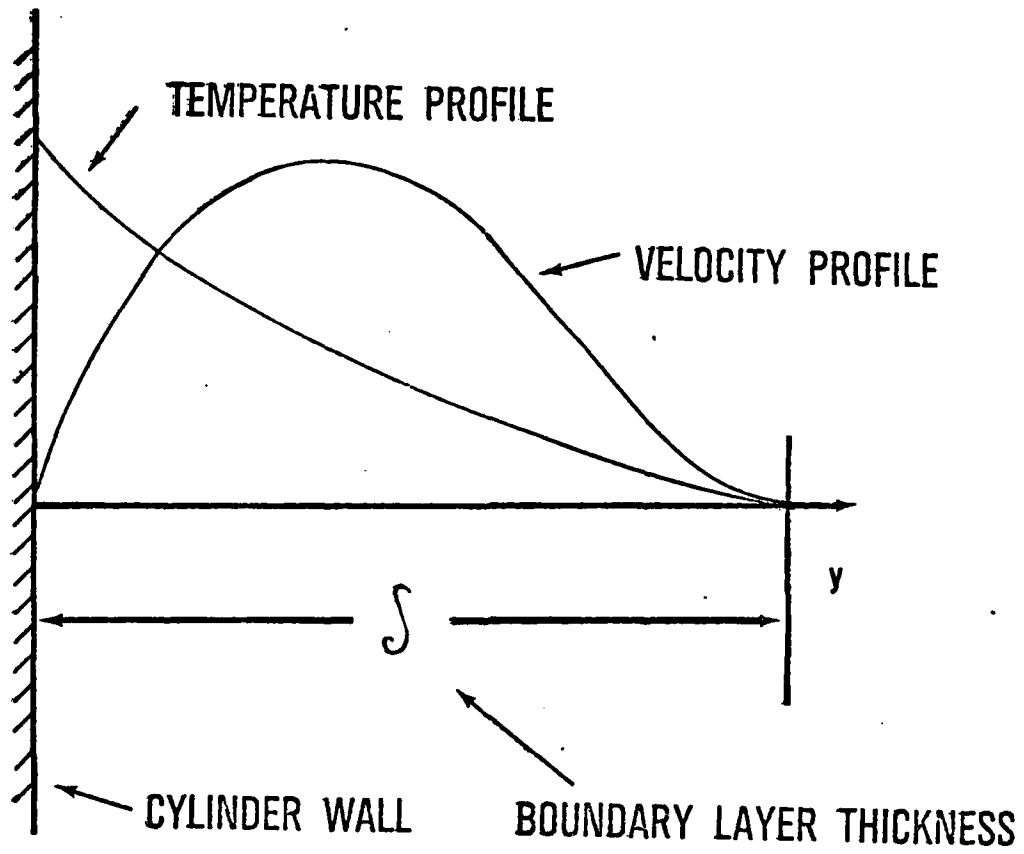


Fig. 10 Assumed Temperature and Velocity Profiles

Equations (37) and (38) are, respectively,

$$\begin{aligned} \frac{1}{x^{+3}} \frac{d}{dx^{+}} \left[x^{+5} \delta^{+} v^{+2} \left(1 + \frac{3}{8} \delta^{+} x^{+} \right) \right] &= \\ &= 140 \delta^{+} x^{+} (1 + 1/4 \delta^{+} x^{+}) - 420 \frac{x^{+} v^{+}}{\delta^{+}} \end{aligned} \quad (39)$$

and

$$\frac{1}{x^{+2}} \frac{d}{dx^{+}} \left[x^{+3} \delta^{+} v^{+} \left(1 + \frac{2}{7} \delta^{+} x^{+} \right) \right] = \frac{240}{Pr \delta^{+}} \quad (40)$$

Upon completion of the differentiation, Eqn (39) is

$$\begin{aligned} x^{+} \delta^{+} v^{+2} \left(1 + \frac{3}{4} x^{+} \delta^{+} \right) \frac{d\delta^{+}}{dx^{+}} + 2x^{+} \delta^{+2} v^{+} \left(1 + \frac{3}{8} x^{+} \delta^{+} \right) \frac{dv^{+}}{dx^{+}} &= \\ = 140\delta^{+2} \left(1 + \frac{1}{4} x^{+} \delta^{+} \right) - 420 v^{+} - 5\delta^{+2} v^{+2} \left(1 + \frac{9}{20} x^{+} \delta^{+} \right) \end{aligned} \quad (41)$$

and Eqn (40) is

$$\begin{aligned} x^{+} \delta^{+} v^{+} \left(1 + \frac{4}{7} x^{+} \delta^{+} \right) \frac{d\delta^{+}}{dx^{+}} + x^{+} \delta^{+2} \left(1 + \frac{2}{7} x^{+} \delta^{+} \right) \frac{dv^{+}}{dx^{+}} &= \\ = \frac{240}{Pr} - 3 \delta^{+2} v^{+} \left(1 + \frac{8}{21} x^{+} \delta^{+} \right) \end{aligned} \quad (42)$$

By defining the following coefficients

$$C_1 = x^{+} \delta^{+} v^{+2} \left(1 + \frac{3}{4} x^{+} \delta^{+} \right)$$

$$C_2 = 2x^{+} \delta^{+2} v^{+} \left(1 + \frac{3}{8} x^{+} \delta^{+} \right)$$

$$C_3 = 140\delta^{+2} \left(1 + \frac{1}{4} x^{+} \delta^{+} \right) - 420 v^{+} - 5\delta^{+2} v^{+2} \left(1 + \frac{9}{20} x^{+} \delta^{+} \right)$$

$$C_4 = x^{+} \delta^{+} v^{+} \left(1 + \frac{4}{7} x^{+} \delta^{+} \right)$$

$$C_5 = x^+ \delta^{+2} \left(1 + \frac{2}{7} x^+ \delta^+\right)$$

$$C_6 = \frac{240}{Pr} - 3\delta^{+2} v^+ \left(\frac{8}{21} x^+ \delta^+ + 1\right)$$

the equation of motion and the energy equation can be written, respectively, as

$$C_1 \frac{d\delta^+}{dx^+} + C_2 \frac{dv^+}{dx^+} = C_3 \quad (43)$$

$$C_4 \frac{d\delta^+}{dx^+} + C_5 \frac{dv^+}{dx^+} = C_6 \quad (44)$$

Initial values for δ^+ and v^+ can be calculated by setting $x^+ = 0$ in the first order differential equation of motion and equation of energy. The two equations can be treated as two simultaneous equations with the two unknowns being δ^+ and v^+ . The resulting equations for the initial conditions are

$$\delta_i^+ = \frac{(240)^{1/2} \left(\frac{20}{21} + Pr\right)^{1/2}}{Pr^{1/2}} \quad (45)$$

$$v_i^+ = \frac{\left(\frac{80}{3}\right)^{1/2}}{\left(\frac{20}{21} + Pr\right)^{1/2}} \quad (46)$$

The initial slopes, i.e. $(d\delta^+/dx^+)_1$ and $(dv^+/dx^+)_1$ can be calculated by evaluating the limit as x^+ approaches zero in the two non-dimensional first order differential equations. Evaluating the limit of the right hand side of Eqn (41) leads to

$$\lim_{x^+ \rightarrow 0} \left(\frac{140\delta^{+2} - 420 v^+ - 5\delta^{+2} v^{+2}}{x^+} \right) =$$

$$= \lim_{x^+ \rightarrow 0} \left(280\delta^+ \frac{d\delta^+}{dx^+} - 420 \frac{dv^+}{dx^+} - 10\delta^+ v^+ \frac{d\delta^+}{dx^+} - 10\delta^{+2} v^+ \frac{dv^+}{dx^+} \right)$$

Combining these terms with the left hand side of Eqn (41) yields the following initial coefficients.

$$C_{1_i} = \delta_i^+ (11 v_i^{+2} - 280)$$

$$C_{2_i} = 12\delta_i^{+2} v_i^+ + 420$$

$$C_{3_i} = \delta_i^{+3} \left(35 - \frac{9}{4} v_i^{+2} \right)$$

Similarly, evaluating the limit of the right hand side of Eqn (42) leads to

$$\lim_{x^+ \rightarrow 0} \left(\frac{240/Pr - 3\delta^{+2} v^+}{x^+} \right) = \lim_{x^+ \rightarrow 0} \left(-3 \frac{d(\delta^{+2} v^+)}{dx^+} \right) =$$

$$= \lim_{x^+ \rightarrow 0} \left(-6\delta^+ v^+ \frac{d\delta^+}{dx^+} - 3\delta^{+2} \frac{dv^+}{dx^+} \right)$$

and combining these terms with the left hand side of Eqn (42) yields the following initial coefficients for the energy equation.

$$C_{4_i} = 7\delta_i^+ v_i^+$$

$$C_{5_i} = 4\delta_i^{+2}$$

$$C_{6_i} = -\frac{8}{7} \delta_i^{+3} v_i^+$$

Finally, the equation of motion, Eqn (41) and the energy equation, Eqn (42) can be solved simultaneously producing

$$\left(\frac{d\delta^+}{dx^+}\right)_i = \frac{C_{3_i}/C_{2_i} - C_{6_i}/C_{5_i}}{C_{1_i}/C_{2_i} - C_{4_i}/C_{5_i}} \quad (47)$$

$$\left(\frac{dv^+}{dx^+}\right)_i = \frac{C_{3_i}/C_{1_i} - C_{6_i}/C_{4_i}}{C_{2_i}/C_{1_i} - C_{5_i}/C_{4_i}} \quad (48)$$

With the information supplied from Eqns (41) through (48) iterative, approximate numerical techniques can be used to find a solution to the coupled non-linear, non-dimensionalized, first order differential equation of motion and energy equation, Eqns (41) and (42), respectively. A numerical technique is outlined in Appendix A.

V. Results and Conclusions

Laminar Region

Quantitative data of the laminar boundary layer region encompassing the vertical cylinder are extracted from Fig 11 using section III and Havener's computational scheme outlined in Ref 11. The wall temperature is 52 C and the ambient temperature is 17 C. The pressure assumed constant through the boundary layer is approximately 0.1 mega-pascals. Using the film temperature to evaluate the properties of air; the Grashof-Prandtl number product, GP , is approximately 3.24×10^7 at $x = .227$ m. Schlichting (Ref 16) theorized laminar flow for $GP < 10^8$.

The fringe shift data extracted from Fig 11, and the polynomial curve fit is shown in Fig 12. A typical temperature profile corresponding to the fringe shift data at $x = .227$ m is shown in Fig 13. In the ambient, the fringe, which is a line of constant optical path length, remains perpendicular to the axis of the cylinder because the density field is constant in this region. However, the fringe deviates in the boundary layer region because the density varies through the boundary layer. The fringe shift provides a direct calculation of this deviation and is a maximum at the cylinder wall where the density of the air is a minimum. For this study, the fringe shifts are calculated along a fringe which means the spatial coordinates of these shifts do not share a common cross-sectional plane. This approach is required to obtain enough data to determine a good fringe shift profile. In theory, the interferometric integral equation applies to planes that are perpendicular to the axis of the cylinder so the shifts should be planar. The non-alignment of the data points with respect to the x-coordinate is small and therefore this approach to measuring the fringe shifts is assumed to be valid.

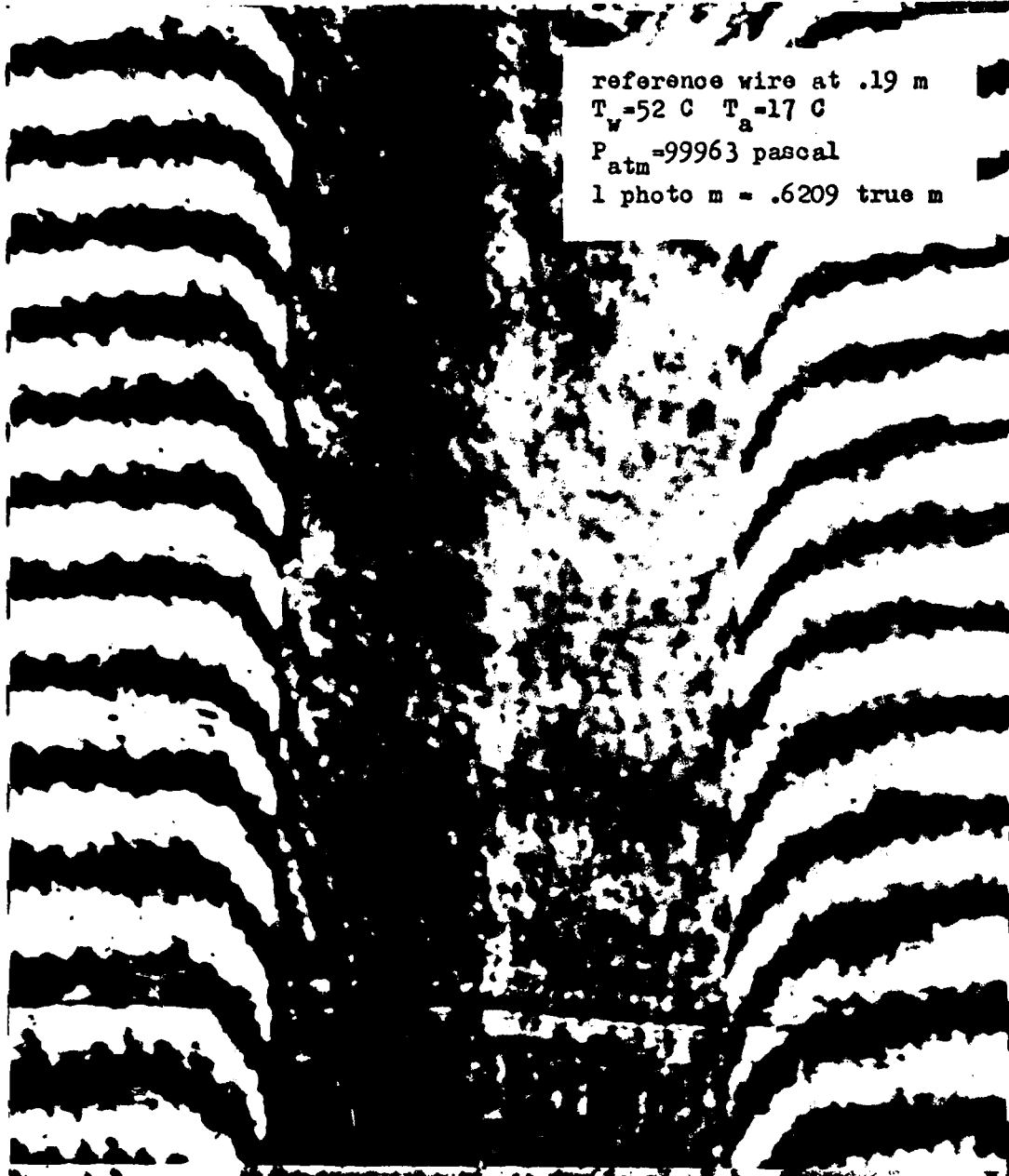


Fig. 11 Finite Fringe Interferogram of Laminar Region
Encompassing Circular Cylinder

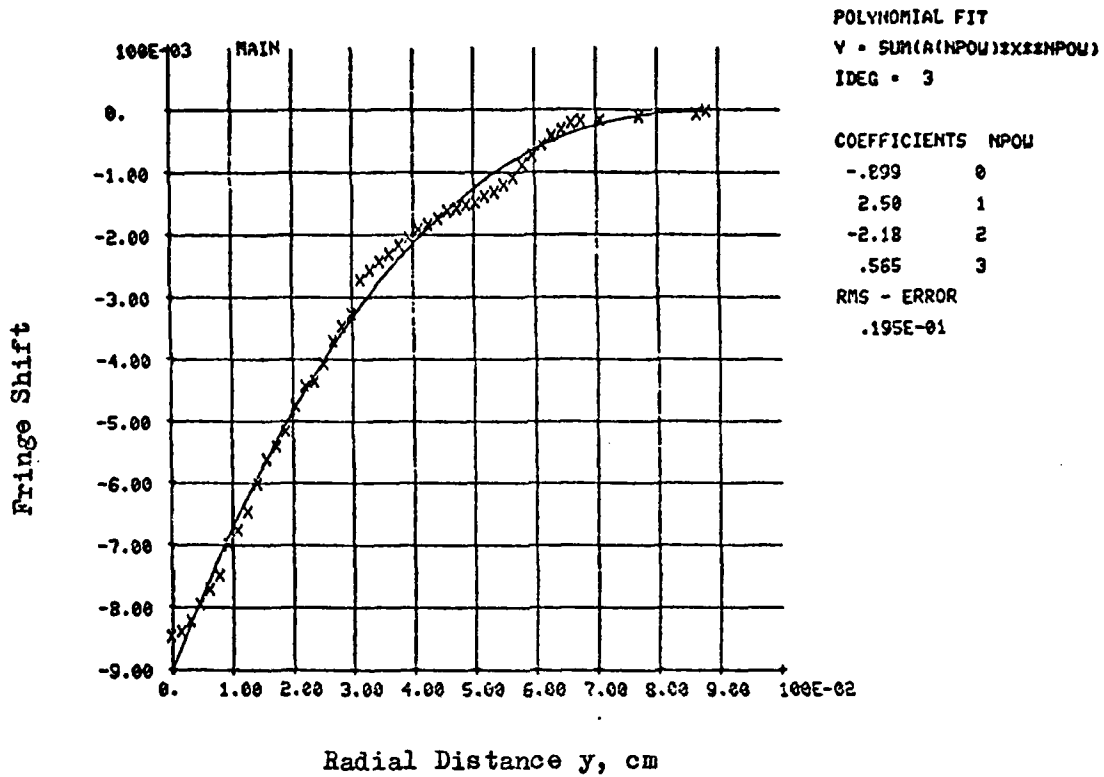


Fig. 12 Quantitative Fringe Shift Data at Radial Distances y

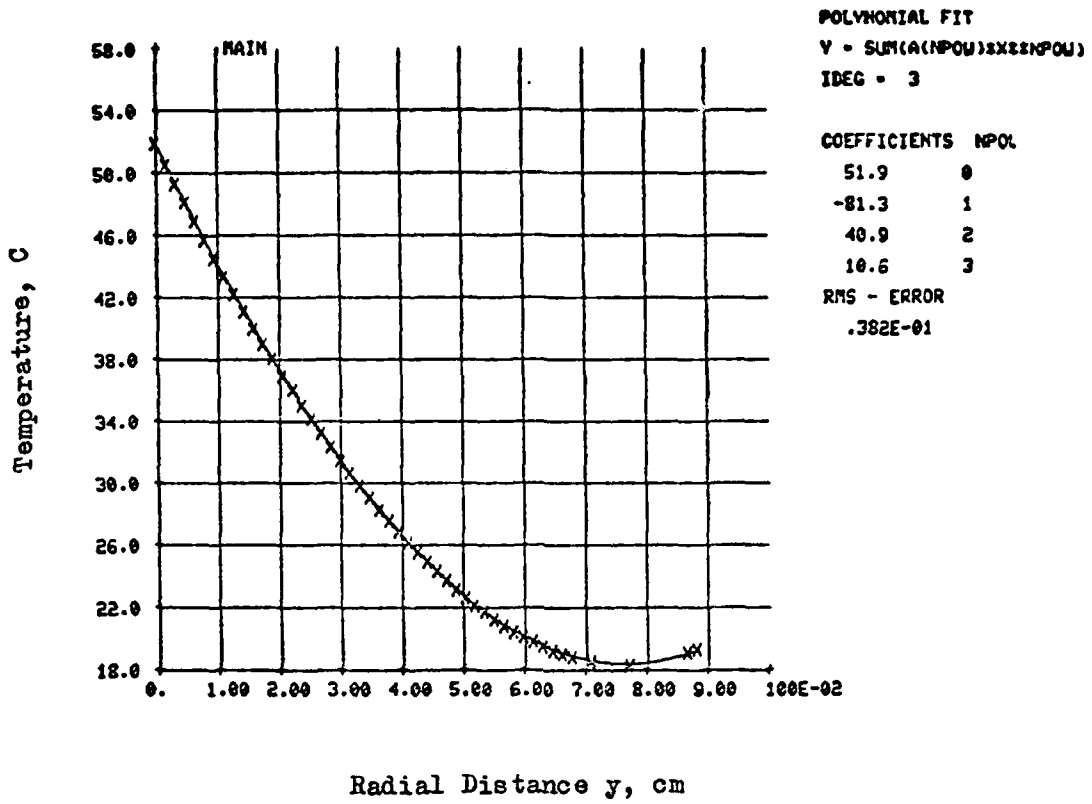


Fig. 13 Temperature Profile in Radial Direction y at $x=.227$ m

The local Nusselt number $(N_{u_x})_{cyl}$ and convective heat transfer coefficient h at $x = .227$ m is calculated using the temperature profile from Fig 13 and the following heat balance equation where $k = 2.888 \times 10^{-4}$ watt/cm-C

$$q_{\text{conduction}} = -k \left(\frac{dt}{dy} \right)_w = q_{\text{convection}} = h(t_w - t_\infty) \quad (49)$$

The convective heat transfer coefficient is 6.73 watt/m²-C. The local Nusselt number

$$(N_{u_x})_{cyl} = \frac{hx}{k} = \frac{\left(\frac{dt}{dy} \right)_w x}{t_w - t_\infty} \quad (50)$$

is approximately 56.9. Using the wall temperature to evaluate the properties of air since $(N_{u_x})_{cyl}$ is proportional to the temperature gradient at the wall; $Gr_x = 3.648 \times 10^7$ and $Pr = .7036$. A theoretical value for $(N_{u_x})_{cyl}$ is taken from the curve $Pr = 0.70$ of Fig 14 which is reproduced from Sparrow's and Gregg's numerical results. The value of ξ at $x = .227$ m is .4016 and $(N_{u_x})_{cyl} / (N_{u_x})_{fp} = 1.18$. The local Nusselt number for the flat plate, $(N_u)_{fp}$ is determined using Eckert's equations.

$$(N_{u_x})_{fp} = 0.508 Pr^{\frac{1}{2}} (0.952 + Pr)^{-\frac{1}{4}} Gr_x^{\frac{1}{4}}$$

$(N_{u_x})_{fp}$ is approximately 31.48 and the theoretical $(N_{u_x})_{cyl}$ is 37.15. The relative disagreement is 34.7 percent between the theoretical and experimental local Nusselt number.

The slope of the numerically derived temperature profile will influence the experimental Nusselt number and the magnitude of disagreement with the theoretical Nusselt number. Error induced in

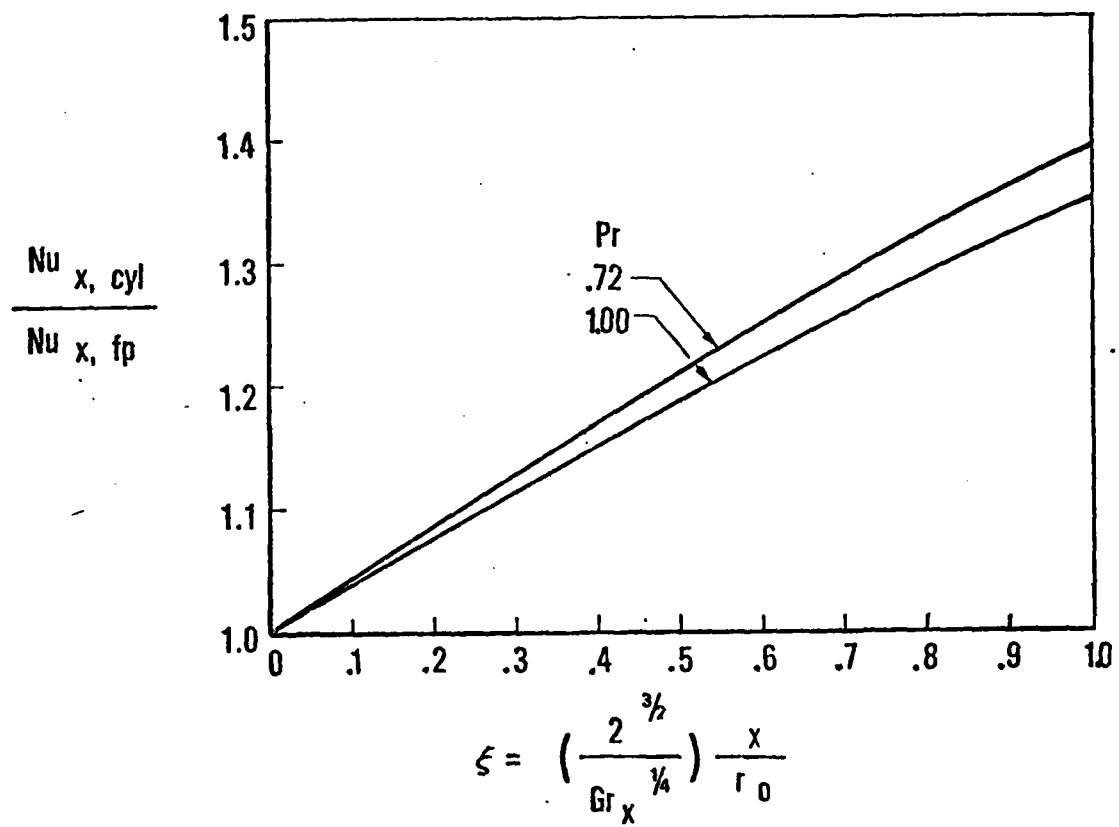


Fig. 14 Comparison of Local Nusselt Number for Cylinder With That for Flat Plate

the experimental fringe shift profile will be magnified in the calculations for a local Nusselt number. More data points would enhance the reliability of the experimental results.

Glassman and Orr (Ref 8) have developed a method to automate the reduction of data from an interferogram. Using a computer and an automated optical scanner, the fringes of an interferogram are digitized and local values of the fringe shift are calculated for variable mesh specifications.

Using this apparatus, an interferogram of the laminar region (Fig 11) is digitized and the local fringe shift values calculated. Subsequently, of these fringe data, a contour map (Ref 1) is produced to obtain lines of constant fringe shift throughout the field. Following this, distributions of fringe shift in planes normal to the axis of the cylinder are determined. From here on, the data reduction process is identical to that previously referenced in this section.

The technique will eliminate error caused by the selection of non-planer data points of a representative cross-sectional area. The spatial coordinates of the relative fringe shifts will share a common cross-sectional plane. Also, the number of data points is increased quite significantly.

Transition Region

Of the three regions for boundary layer analysis, transition is the least understood. An attempt is made to better understand the transition region both qualitatively and quantitatively.

Schlichting uses the following criteria for the Grashof-Prandtl number product to define the transition region,

$$10^8 < GP < 10^{10}$$

Figure 15 is the result of an interferogram of the vertical cylinder and boundary layer for a wall temperature of 127 C and an ambient temperature of 19 C. Using the film temperature to evaluate the relevant properties of air and selecting a point on the cylinder corresponding to the middle of Fig 15, the Grashof-Prandtl number product is calculated to be approximately 9.2×10^9 .

It is interesting to note the existence of fringe reversal next to the cylinder wall in Fig 15. One possible explanation for the fringe reversal is as follows. In the transition region, the flow begins to become unstable. The instability at the onset of transition is caused by small perturbations. The perturbations may be due to forces or momentum fluxes contributed by the ambient surroundings. These perturbations can strengthen and cause the boundary layer thickness to fluctuate. At the onset of transition the amplitude of the fluctuation is small and increases in magnitude as the turbulent region is approached.

For laminar flow, the gradients for temperature and density are the steepest at the wall. The gradients are also the steepest for this region as compared to the transition and turbulent regions. The fluctuation of the boundary layer thickness in the transition region influences the

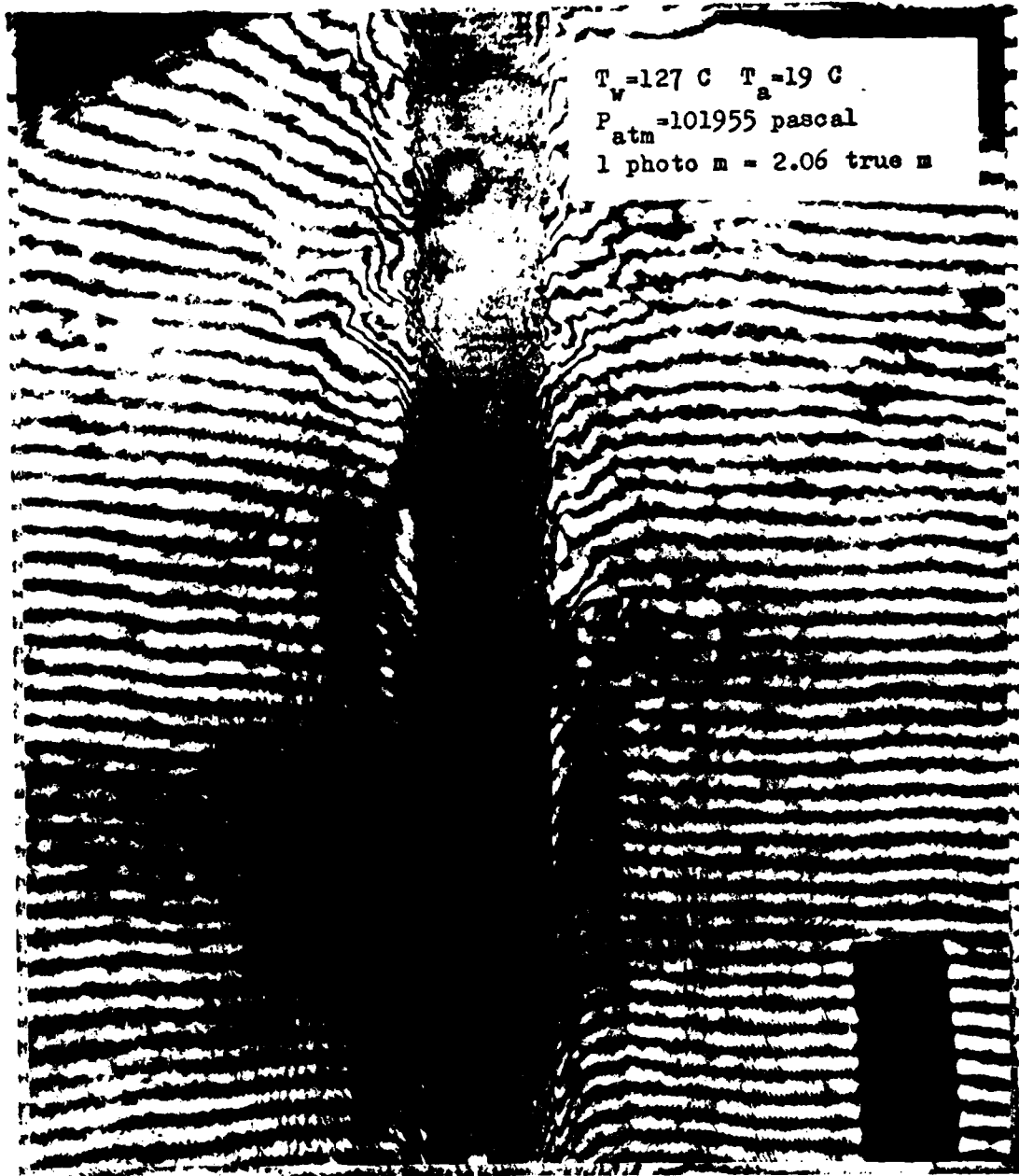


Fig. 15 Finite Fringe Interferogram of Transition Region Encompassing Circular Cylinder

steepness of the gradients because they depend on the boundary layer thickness for convective heat exchange.

The fringes are lines of constant optical path length. The optical path length is proportional to the index of refraction integrated over a finite path length. For a gas the index of refraction is proportional to density. So the optical path length is proportional to the density which is inversely proportional to temperature. A change in the steepness of the density and temperature gradients influences the shape of the fringes in an interferogram. The fringe reversal in Fig 15 shows this change in the density profile.

The fringe reversal can also be observed in Fig 11 of the laminar boundary layer region. These qualitative results suggest that the fringe reversal may be evidence of the phenomena that causes laminar flow to transition to turbulent flow.

In Fig 15, the fringe reversal appears to be non-axisymmetric. This may be caused by a slight tilt in the cylinder axis with respect to true vertical. Havener (Ref 11), has suggested a method to calculate the error of a non-axisymmetric fringe shift compared to an axisymmetric case. Appendix B contains information on this error analysis. Using Havener's method, the possible error incurred here is 3 percent.

The qualitative data obtained in this investigation supports the theory that the flow is periodic. The characteristics of the transition flow appear to represent wave phenomena.

Figure 16 is a zeroth fringe interferogram of the top portion of the vertical cylinder and free convection condition as shown in Fig 15. The boundary layer is non-laminar as indicated by the erratic interference pattern. The boundary layer thickness varies randomly in this



Fig. 16 Zeroth Fringe Interferogram of Transition Region Encompassing Circular Cylinder

region and there are locations where the flow appears to resume or imitate a laminar flow. Figure 17 shows the same conditions as Fig 16 except the interference pattern is now a finite fringe pattern. This random interference pattern of the transition boundary layer means the optical path length is varying rapidly in this region. A qualitative assessment of this condition is that the density is also varying rapidly but not randomly; while the local pattern is erratic and indicates the existence of steep gradients, there also appears to be a wave structure throughout this section of the transition region. Superposition of Figs 16 and 17 outlines this section of the transition boundary layer and reveals qualitatively this wave phenomena.

For this investigation, since each interferogram is an instantaneous record of the flow, transient phenomena is difficult to identify in a single exposure. Accordingly, data of the wave phenomena can be extracted from a motion picture film of the transition boundary layer. Schlieren color photographs of the transition region reproduced from motion picture film exposed at 500 frames per second are presented in Figs 18 through 34. Every tenth frame has been enlarged and printed for qualitative assessment of the wave structure; these color enlargements definitely suggest that this transition flow is periodic. Each disturbance (a wave) that propagates along the cylinder wall appears to be followed by a new disturbance that follows the so called tracks of the previous disturbance. This periodic phenomenon is visible by comparing the first and eighth photographs where the new disturbance can be seen as a replacement to the old disturbance.

As a disturbance propagates* along the cylinder wall, a vortex is seen to be created and shed. The boundary layer flow separates into

* Observed in movie of boundary layer presented with thesis.



Fig. 17 Finite Fringe Interferogram of Transition
Region Encompassing Circular Cylinder

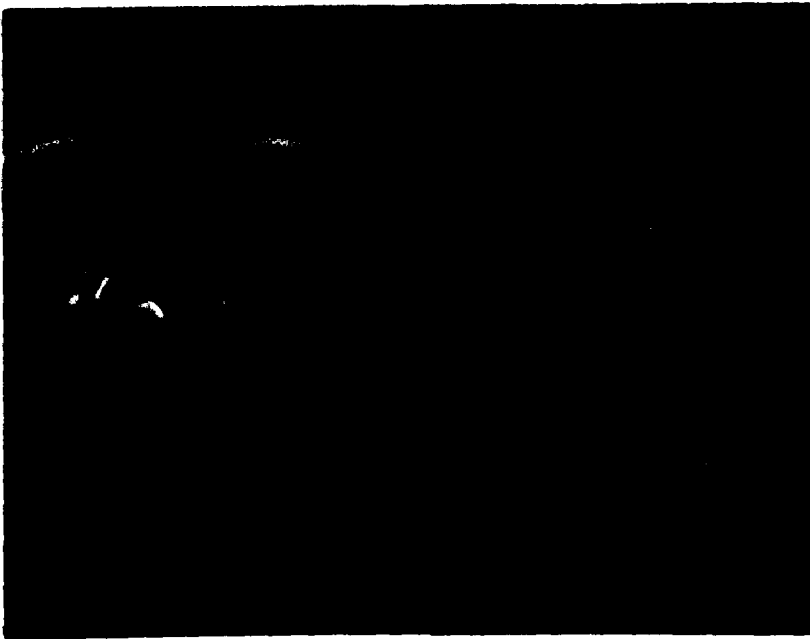


Fig. 18 t=0 sec

reference wire
at 1.16 m
 $T_w = 176\text{ C}$ $T_a = 22\text{ C}$
 $P_{atm} = 101280\text{ pascal}$

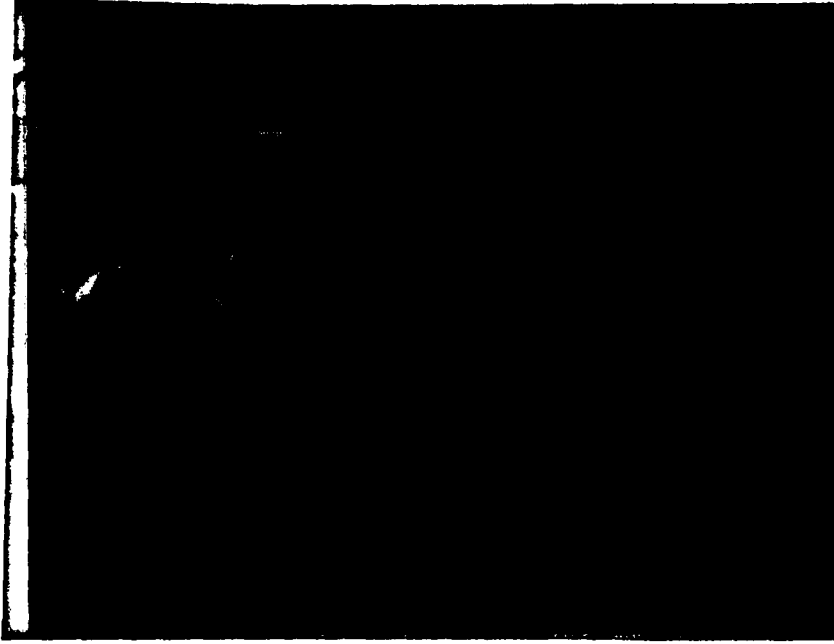


Fig. 19 t=.02 sec

Figs. 18-34 Schlieren Color Photographs of Transition Region.

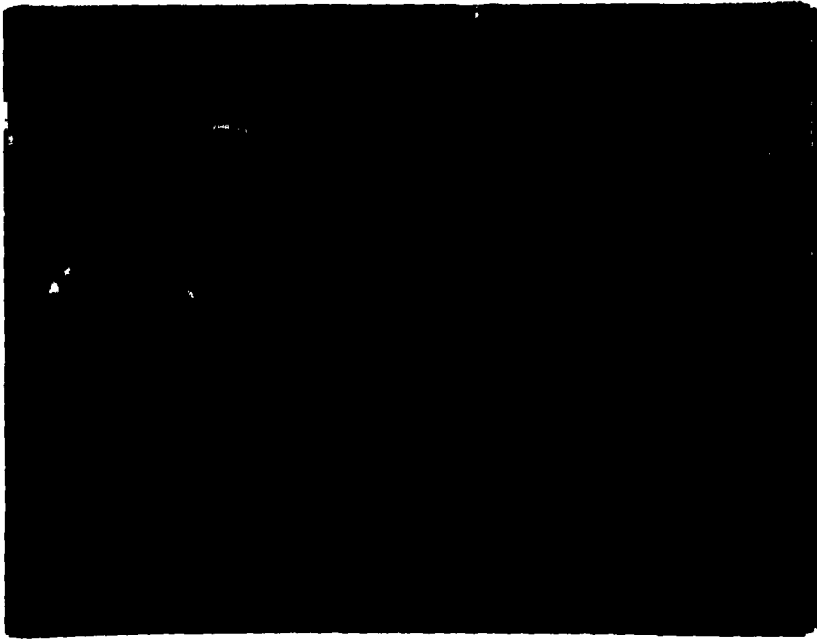


Fig. 20 $t=.04$ sec



Fig. 21 $t=.06$ sec

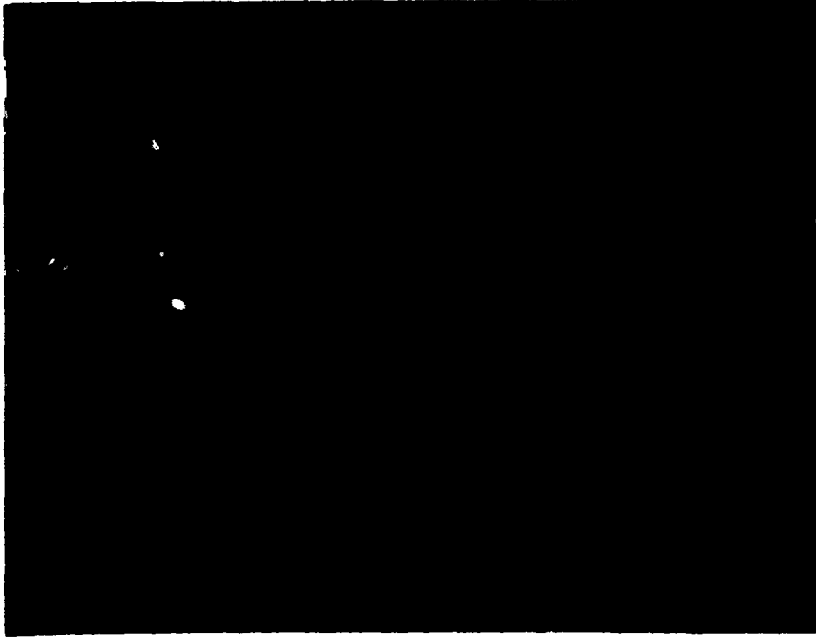


Fig. 22 $t=0.08$ sec



Fig. 23 $t=0.10$ sec

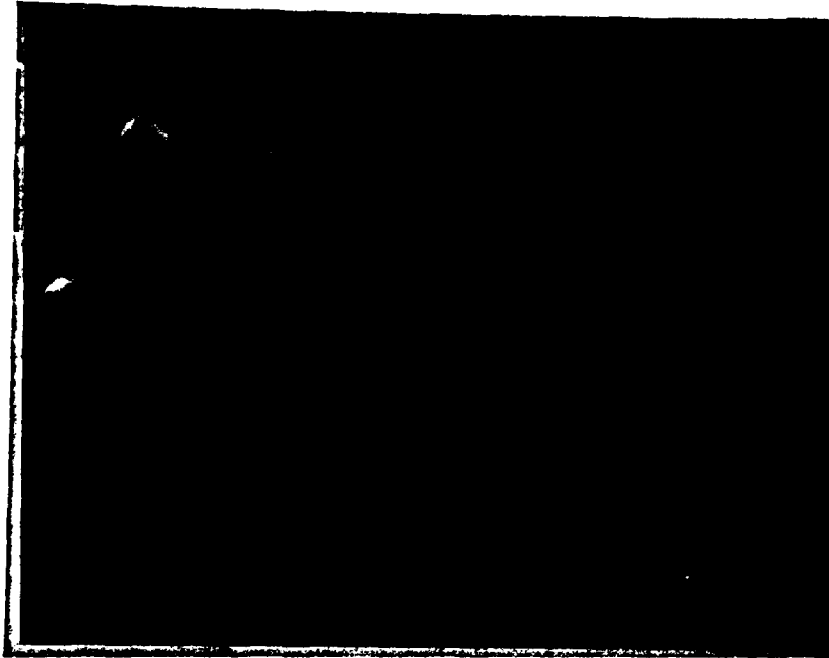


Fig. 25 $t=.14$ sec



Fig. 24 $t=.12$ sec



Fig. 27 $t=0.18$ sec



Fig. 26 $t=0.16$ sec

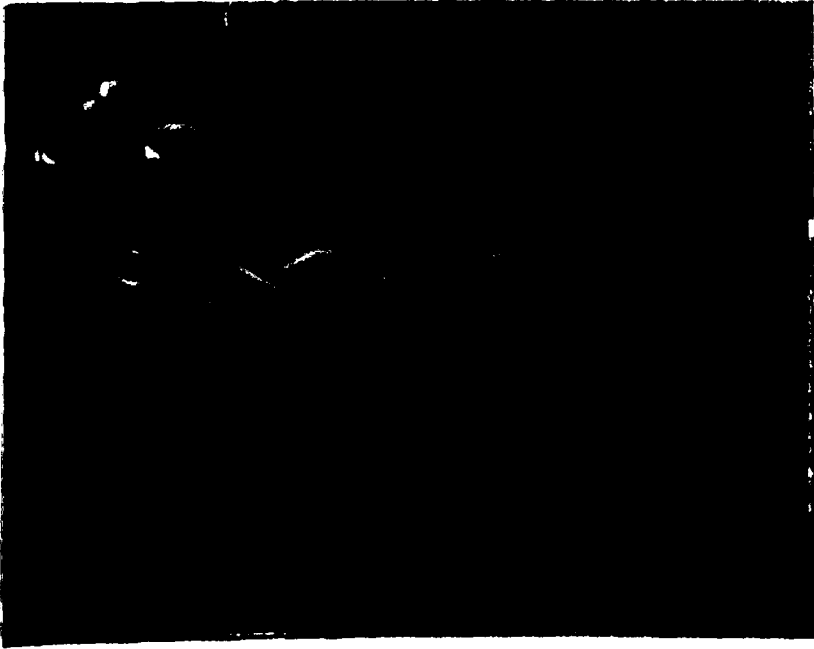


Fig. 28 $t=0.20$ sec

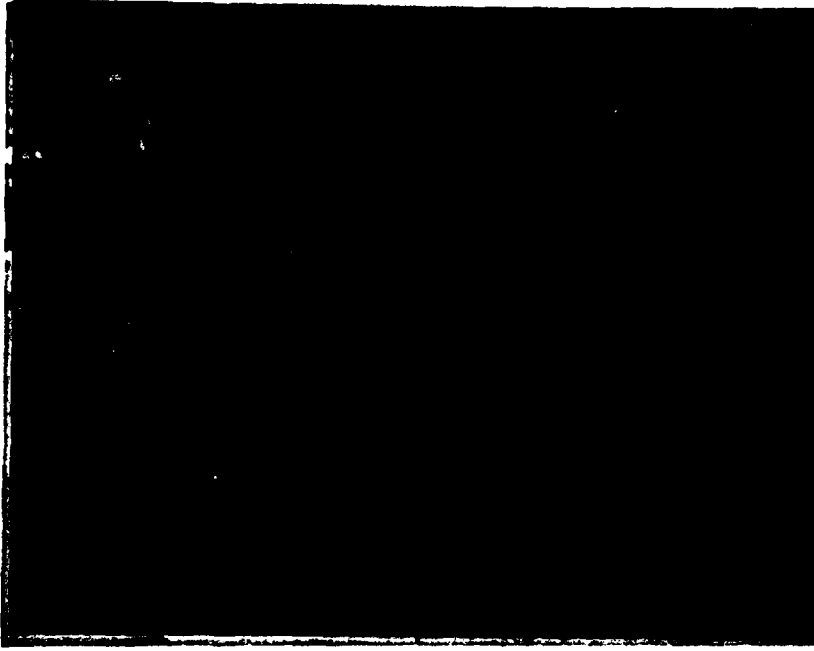


Fig. 29 $t=0.22$ sec

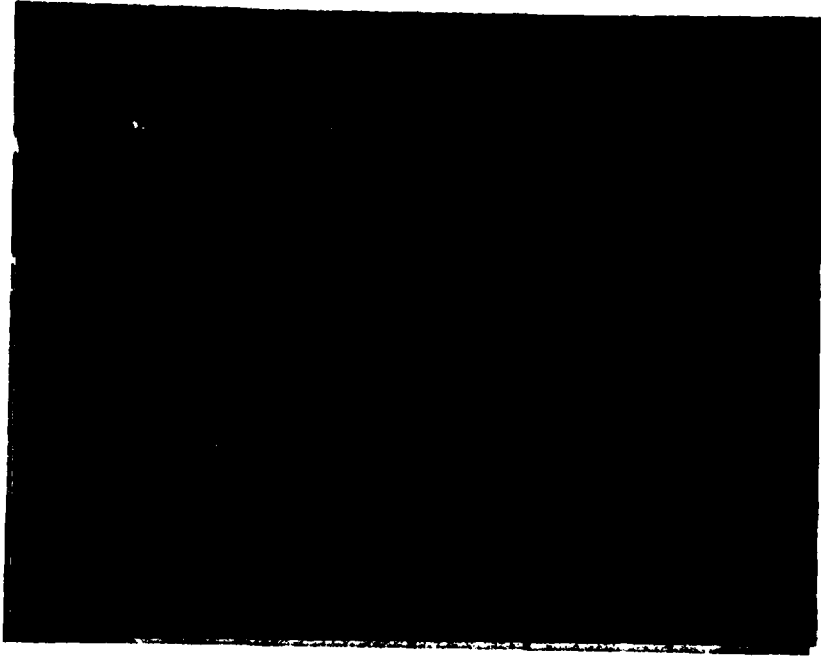


Fig. 31 $t = .26$ sec

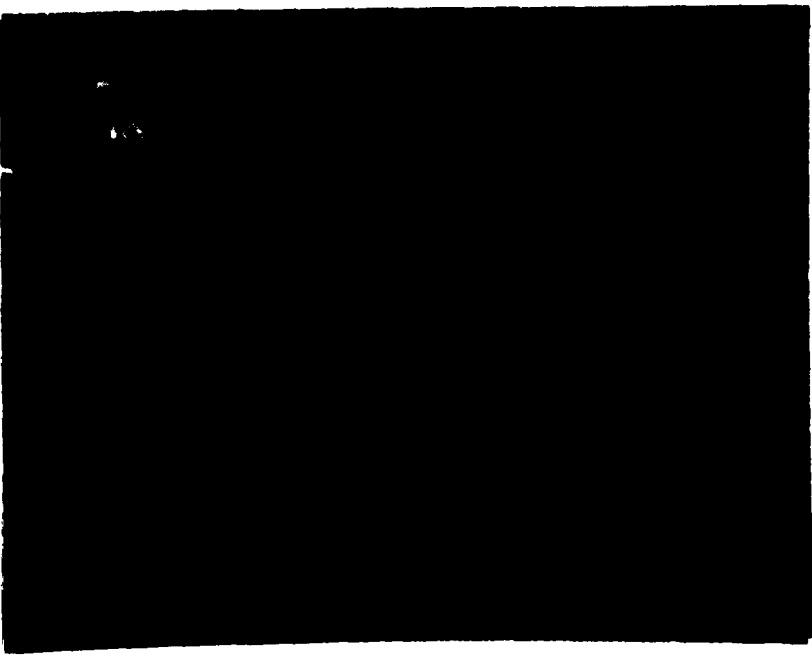


Fig. 30 $t = .24$ sec

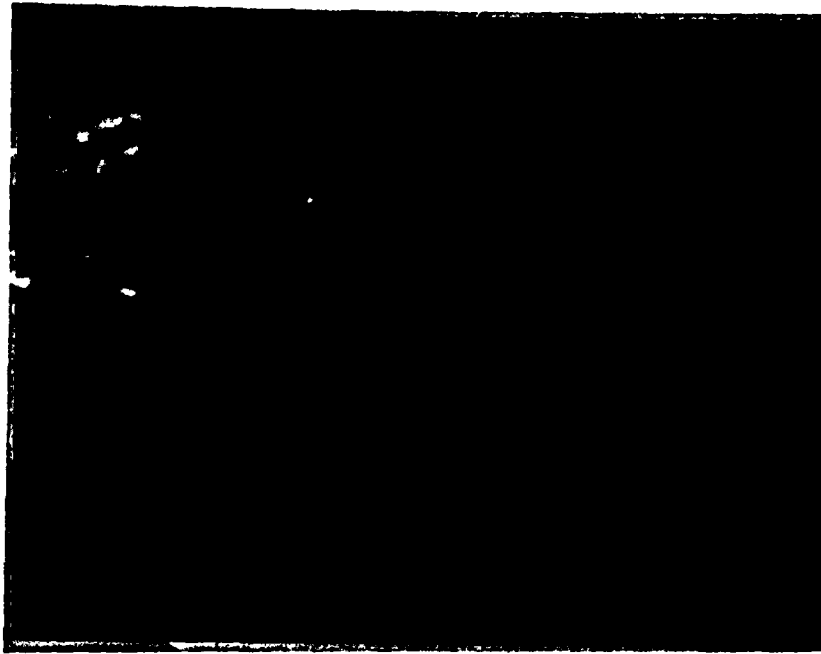


Fig. 33 $t = .30$ sec.

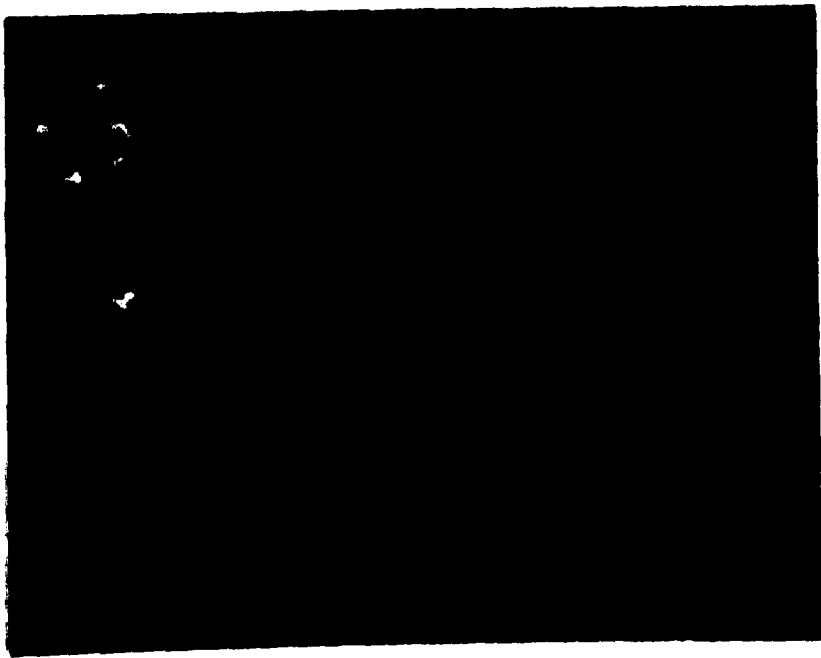


Fig. 32 $t = .28$ sec.

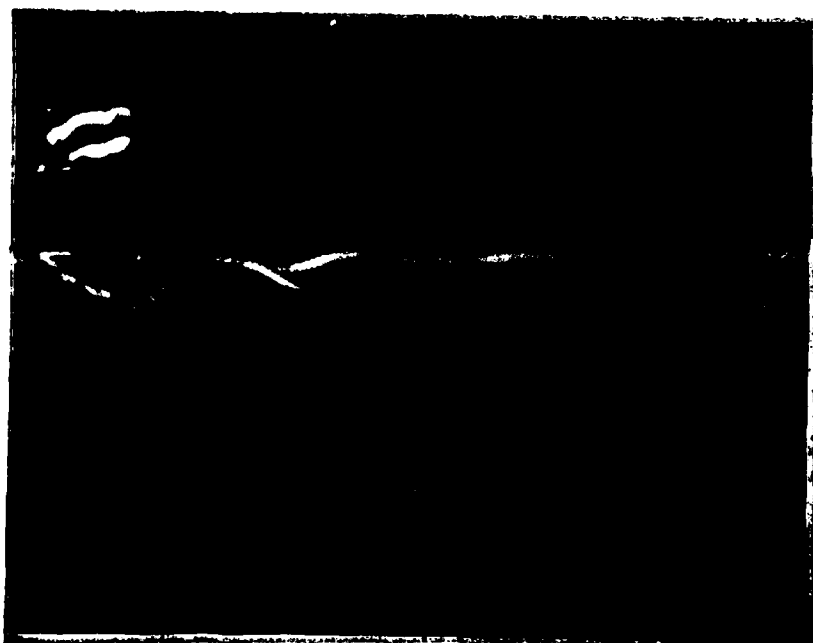


Fig. 34 $t=0.32$ sec

individual mass packets and some of the packets form into the vortex. The vortices are periodic and start and terminate at a prescribed location. It is the author's belief that the vortices are caused by a momentum flux of air passing from the ambient to replace the warmer air that has dissipated into the ambient surroundings due to the shed vortices.

The special fringe reduction technique discussed for the laminar region could be extended to the transition region. A good quantitative assessment of the transition region could be achieved.

Future Recommendations

In a method developed by Havener (Ref 2), a computer is used to produce finite fringe interferograms from theoretical density distributions of a field. These computational interferograms are compared to actual test interferograms to see how well the two agree. If the agreement is good, the theoretical density field may be assumed to be the same as the actual field; which means the density has been determined without actually reducing experimental interferometric data. For the case studied in this research, the solution to the set of first order, non-linear differential equations or the solutions presented by Cebeci and Sparrow and Gregg could be used to produce computational interferograms. The computational interferograms could be compared to the test interferograms to confirm the numerical solutions.

Also in future efforts, the contour mapping technique could be extended to analysing the turbulent region. If a density function describing the turbulent region is obtained, Havener's method could be utilized to prepare computational interferograms. The information obtained would aid in the understanding of turbulent flow phenomena.

Bibliography

1. A General Purpose Contouring Program, GPCP-II. California: California Computer Products, Inc., 1972.
2. "A Methodology for Producing Computational Interferograms." AFFDL Technical Report to be published March 1980.
3. Cebeci, Tuncer and A. M. O. Smith. Analysis of Turbulent Boundary Layers. New York: Academic Press, 1974.
4. Cebeci, Tuncer. "Laminar-Free-Convective-Heat Transfer from the Outer Surface of a Vertical Slender Circular Cylinder." Heat Transfer, Vol I, #14 (1974).
5. Dean, R. C., Jr. Aerodynamic Measurements. Cambridge: Massachusetts Institute of Technology, 1953.
6. Dudley, David D. Holography, A Survey. NASA, Washington D.C., 1973.
7. Eckert, E. R. G. Heat and Mass Transfer. New York: McGraw-Hill Book Company, Inc., 1959.
8. Glassman, A. T. and C. E. Orr. "Automated Interferogram Reduction." Ohio: University of Dayton Research Institute, 1979.
9. Gregg, J. L. and E. M. Sparrow. "Laminar-Free-Convection Heat Transfer from the Outer Surface of a Vertical Circular Cylinder." Transactions of the ASME, Vol 78, #8 (Nov 1956).
10. Havener, A. G. "A User's Guide on Pulse Laser Holography for Wind Tunnel Testing." USAF ARL TR 75-0213, 1975.
11. Private Communication.
12. Kays, W. M. Convective Heat and Mass Transfer. New York: McGraw-Hill Book Company, Inc., 1966.
13. McAdams, W. H. Heat Transmission. New York: McGraw-Hill Book Company, Inc., 1954.

14. Merzkirch, Wolfgang. "Generalized Analysis of Shearing Interferometers as Applied for Gas Dynamic Studies." Applied Optics, Vol 13, (Feb 1974).
15. Ostrovskiy, Yu I. "Holography." NASA Technical Translation, NASA TT F-706 (May 1972).
16. Schlichting, H. Boundary Layer Theory. New York: McGraw-Hill Book Co., Inc., 1966.
17. Trolinger, J. D. "Laser Instrumentation for Flow Field Diagnostics," Advisory Group for Aerospace Research and Development, AGARD-AG-186, (Mar 1974).

Appendix A

Approach for Numerical Solution of Governing System of Equations

An iterative technique is used to obtain a numerical approximation for the non-dimensional boundary layer thickness, δ^+ . The same procedure is also used to obtain an approximation for the non-dimensional velocity, v^+ . Both of these parameters are functions of only the Prandtl number Pr and the non-dimensional axial coordinate, x^+ .

The following two equations are used to obtain δ^+ and v^+ at $(x^+ + \Delta x^+, n)$,

$$\delta_n^+ = \left(\frac{d\delta^+}{dx^+} \right)_{n-1} \Delta x^+ + \delta_{n-1}^+ \quad (A-1)$$

$$v_n^+ = \left(\frac{dv^+}{dx^+} \right)_{n-1} \Delta x^+ + v_{n-1}^+ \quad (A-2)$$

Here, $n-1$ denotes the initial values at $x^+ = 0$.

After values for δ_n^+ and v_n^+ are known at the new station n , values for the slopes $(d\delta^+/dx^+)_n$ and $(dv^+/dx^+)_n$ are calculated. Knowing the values of δ^+ , v^+ , $d\delta^+/dx^+$, and dv^+/dx^+ at two stations, a third degree polynomial numerical approximation is used to calculate better values for δ^+ and v^+ at a third station $n+1$ which is another station incremented from n by Δx^+ . The general form of the polynomials used are

$$\delta_{n+1}^+ = a + b x_{n+1}^+ + c x_{n+1}^{+2} + d x_{n+1}^{+3} \quad (A-3)$$

and

$$v_{n+1}^+ = a' + b' x_{n+1}^+ + c' x_{n+1}^{+2} + d' x_{n+1}^{+3} \quad (A-4)$$

Figure A-1 displays the three stations. The value for δ_{n+1}^+ can be evaluated because δ_n^+ , δ_{n-1}^+ , $d\delta_n^+/dx_n^+$, and $d\delta_{n-1}^+/dx_{n-1}^+$ are known at two previous stations. Next, the coefficients in Eqn (A-3) are evaluated from

$$d = \frac{(x_n^+ - x_{n-1}^+) \left[\left(\frac{d\delta^+}{dx^+} \right)_n + \left(\frac{d\delta^+}{dx^+} \right)_{n-1} \right] - 2(\delta_n^+ - \delta_{n-1}^+)}{(x_n^+ - x_{n-1}^+)^3}$$

$$c = \frac{\left[\left(\frac{d\delta^+}{dx^+} \right)_n - \left(\frac{d\delta^+}{dx^+} \right)_{n-1} \right] - 3(x_n^{+2} - x_{n-1}^{+2})d}{2(x_n^+ - x_{n-1}^+)}$$

$$b = \left(\frac{d\delta^+}{dx^+} \right)_{n-1} - 2cx_{n-1}^+ - 3dx_{n-1}^{+2}$$

$$a = \delta_{n-1}^+ - bx_{n-1}^+ - cx_{n-1}^{+2} - dx_{n-1}^{+3}$$

after which Eqn (A-3) is used to calculate δ^+ at station $n+1$ or δ_{n+1}^+ . The same procedure is used to calculate the coefficients in Eqn (A-4) and v^+ at station $n+1$ is also calculated. Next, the slopes $(d\delta^+/dx^+)_{n+1}$ and $(dv^+/dx^+)_{n+1}$ are calculated using the pair of coupled equations, Eqns (43) and (44). The values at stations $n+1$ and n are subsequently used to calculate new values at the next station which is a Δx^+ increment away. Repeated use of this numerical approach is carried out for all Δx^+ increments over the cylinder length.

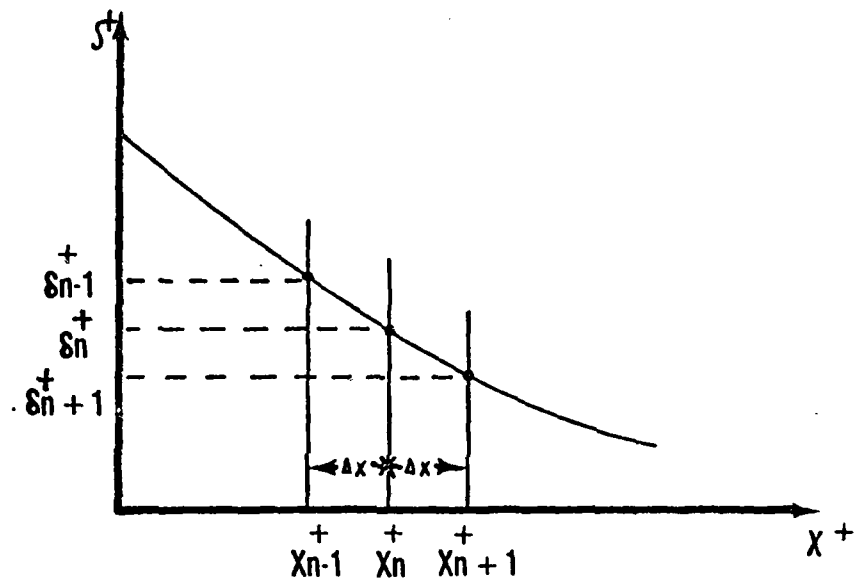


Fig. A-1 Stations for Polynomial Numerical Approximation

The coupled equations, Eqns (43) and (44) are a set of non-linear first order differential equations. For that reason, the numerical approximations for δ^+ , v^+ , $d\delta^+/dx^+$ and dv^+/dx^+ are highly sensitive to the coefficients in Eqns (A-3), (A-4), (43) and (44). The coupled equations are also singular at $x^+ = 0$. Further understanding of Eqns (43) and (44) is required to obtain correct numerical profiles for δ^+ and v^+ .

Appendix B

Error Analysis

From the comparison of an elliptic density field of eccentricity e to that of a circular axisymmetric density field, Havener (Ref 11), developed the following equation in the analysis of the error in the fringe shift equation (Eqn 1) due to a non-axisymmetric density field.

$$S(y)_e = \sqrt{1 - e^2} S(y)_o \quad (B-1)$$

$S(y)_e$ is the fringe shift corresponding to the i th path through a non-axisymmetric elliptic density field and $S(y)_o$ is the fringe shift corresponding to the i th path through an axisymmetric circular density field. The cross-section of the axisymmetric density field is a circle that is concentric with the ellipse of the cross-section of the non-axisymmetric density field. The circle is of minimum radius required to encompass the ellipse.

If an elliptic density field is assumed to be axisymmetric the error incurred would be

$$\text{error} = (1 - \sqrt{1 - e^2}) \times 100 \quad (B-2)$$

For an error analysis of this investigation Fig 15 of the transition region is used. Measuring from the cylinder axis to the edge of the boundary layer (measured at the reference wire) the left side yields $b = 1.75$ units and for the right side $a = 1.70$ units. Assuming the cross-sectional area of the density field to be elliptic; the eccentricity of the ellipse is $e = .24$ and the error induced would be approximately 3 percent.

A slight tilt in the cylinder axis will not necessarily result in an elliptic, non-axisymmetric density field. The cross-sectional area of the density field for this investigation is assumed to be axisymmetric so that only one view is required to examine the density field. Multiple views are required to determine the shape of the cross-sectional area of an asymmetric field. Since instantaneous multiple views are impossible to obtain for this study; the assumed elliptic shape of the cross-sectional area of the density field leads to an approximate 3 percent error in the data reduction of the fringe shift. In the scope of experimental investigations, this error is tolerable.

Vita

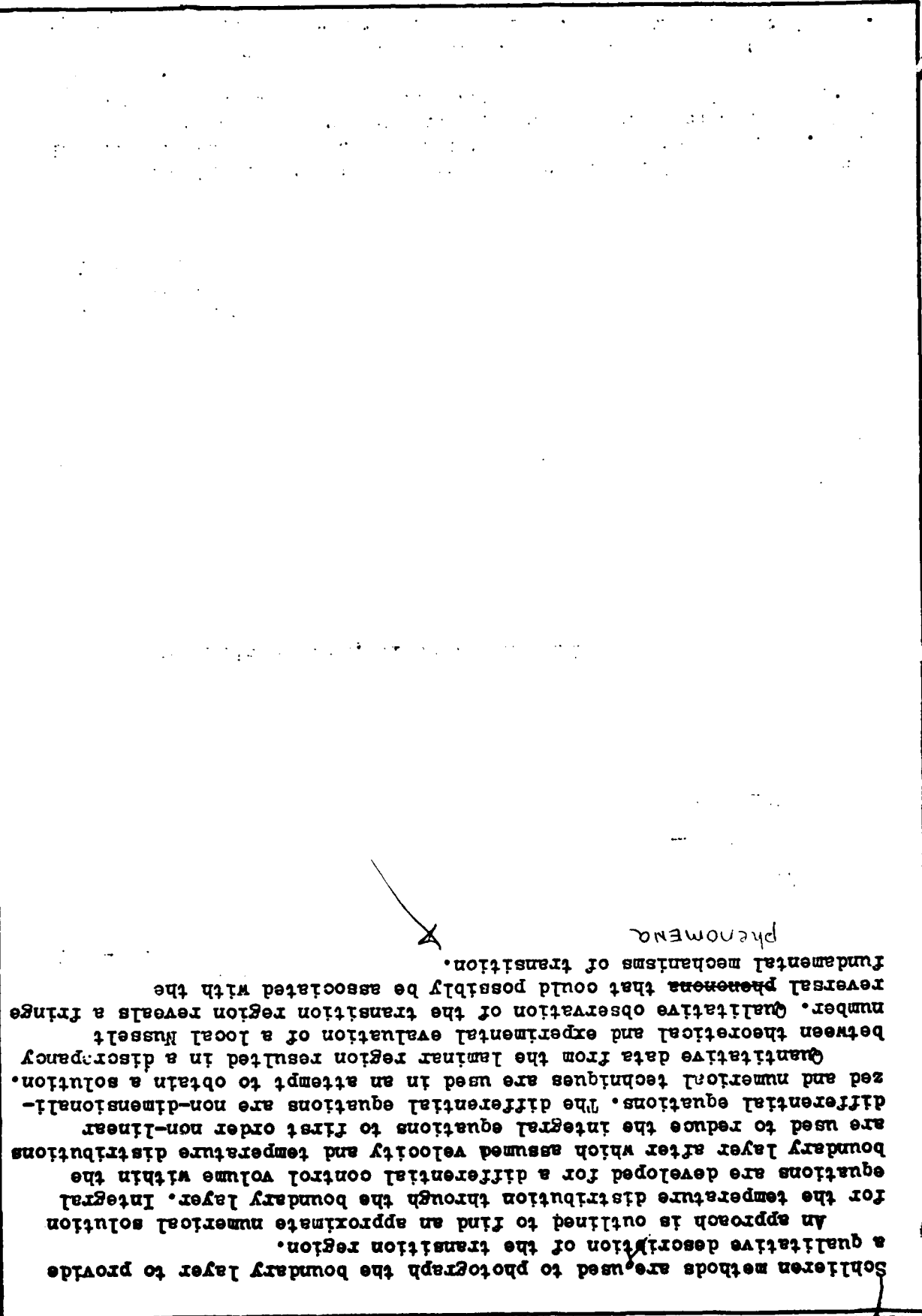
Gregory S. Meserve was born 25 February 1955 in Berlin, New Hampshire. He graduated from Gorham High School, Gorham, New Hampshire in 1973. Upon completion of his freshman year at Boston University, Boston, Massachusetts he enlisted in the Air Force. After 14 months of service he was awarded a three year ROTC scholarship at the University of New Hampshire, Durham, New Hampshire. Just prior to graduation and receiving a B. S. in Mechanical Engineering, Lt. Meserve was accepted for enrollment to the Air Force Institute of Technology.

Permanent Address: Jackson, New Hampshire.

UNCLASSIFIED

SECURITY CLASSIFICATION OF THIS PAGE (When Data Entered)

REPORT DOCUMENTATION PAGE		READ INSTRUCTIONS BEFORE COMPLETING FORM
1. REPORT NUMBER AFIT/GAE/AA/79D-12 ✓	2. GOVT ACCESSION NO.	3. RECIPIENT'S CATALOG NUMBER
4. TITLE (and Subtitle) HOLOGRAPHIC INTERFEROMETRIC SURVEY OF BOUND- ARY LAYER TRANSITION IN AN AXISYMMETRIC FREE CONVECTION THERMAL BOUNDARY LAYER		5. TYPE OF REPORT & PERIOD COVERED MS Thesis
7. AUTHOR(s) Gregory S. Meserve		6. PERFORMING CRG. REPORT NUMBER
9. PERFORMING ORGANIZATION NAME AND ADDRESS Air Force Institute of Technology (AFIT-ENA) Wright-Patterson AFB, Ohio 45433		8. CONTRACT OR GRANT NUMBER(s)
11. CONTROLLING OFFICE NAME AND ADDRESS		10. PROGRAM ELEMENT, PROJECT, TASK AREA & WORK UNIT NUMBERS
14. MONITORING AGENCY NAME & ADDRESS (if different from Controlling Office)		12. REPORT DATE December, 1979
		13. NUMBER OF PAGES 62
		15. SECURITY CLASS. (of this report) Unclassified
		15a. DECLASSIFICATION/DOWNGRADING SCHEDULE
16. DISTRIBUTION STATEMENT (of this Report) Approved for public release; distribution unlimited JOSEPH P. HIPPS, Major, USAF Director of Public Affairs		
17. DISTRIBUTION STATEMENT (of the abstract entered in Block 20, if different from Report)		
18. SUPPLEMENTARY NOTES		
19. KEY WORDS (Continue on reverse side if necessary and identify by block number) Pulse Laser Holography Free Convection Vertical Cylinder Thermal Boundary Layer		
20. ABSTRACT (Continue on reverse side if necessary and identify by block number) Unique optical data from the laminar and transition regions of an axisymmetric free convection thermal boundary layer are presented. The boundary layer encompasses a vertically oriented right circular cylinder kept at a constant wall temperature and suspended in a quiescent air environment. Pulse laser holographic interferometry was used to obtain a measurement of the temperature distribution through the boundary layer.		



PHENOMENA

Schlieren methods are used to photograph the boundary layer to provide a qualitative description of the transition region. An approach is outlined to find an approximate numerical solution for the temperature distribution through the boundary layer. Integral equations are developed for a differential control volume within the boundary layer after which assumed velocity and temperature distributions are used to reduce the integral equations to first order non-linear differential equations. The differential equations are non-dimensionalized and numerical techniques are used in an attempt to obtain a solution. Quantitative data from the laminar region resulted in a discrepancy between theoretical and experimental evaluation of a local Nusselt number. Qualitative observation of the transition region reveals a fringe reversal phenomena that could possibly be associated with the fundamental mechanisms of transition.

Schlieren methods are used to photograph the boundary layer to provide a qualitative description of the transition region.

An approach is outlined to find an approximate numerical solution for the temperature distribution through the boundary layer. Integral equations are developed for a differential control volume within the boundary layer after which assumed velocity and temperature distributions are used to reduce the integral equations to first order non-linear differential equations. The differential equations are non-dimensionalized and numerical techniques are used in an attempt to obtain a solution.

Quantitative data from the laminar region resulted in a discrepancy between theoretical and experimental evaluation of a local Nusselt number. Qualitative observation of the transition region reveals a fringe reversal phenomena that could possibly be associated with the fundamental mechanisms of transition.

phenomena